On the Origin of Enhanced Tempering Resistance of the Laser Additively Manufactured Hot Work Tool Steel in the As-Built Condition

(article starts on next page)

On the Origin of Enhanced Tempering Resistance of the Laser Additively Manufactured Hot Work Tool Steel in the As-Built Condition

FARAZ DEIRMINA, SASAN AMIRABDOLLAHIAN, GRETA LINDWALL, ALBERTO MOLINARI, JITENDAR KUMAR TIWARI, EDUARD HRYHA, and MASSIMO PELLIZZARI
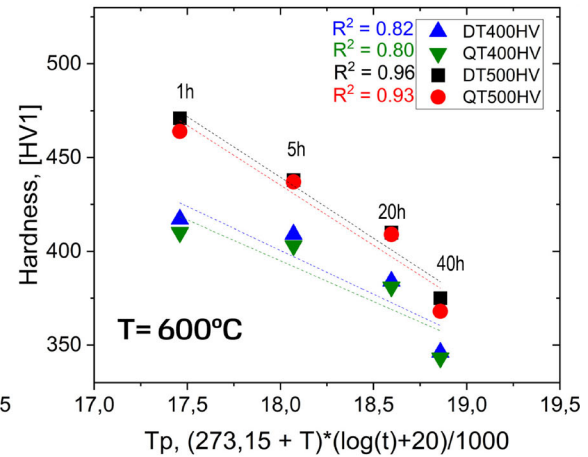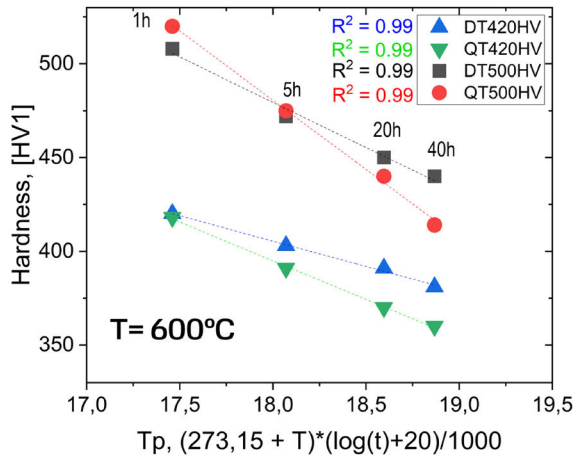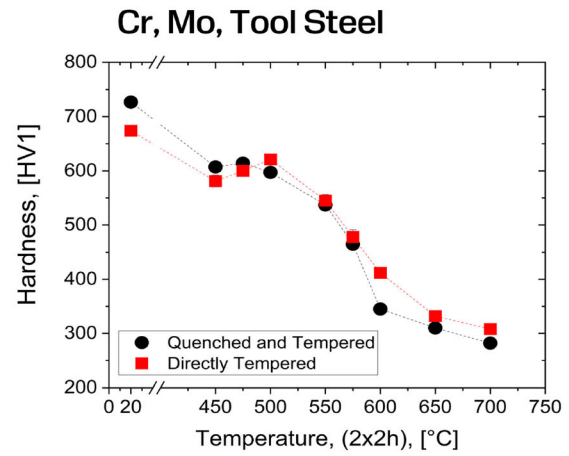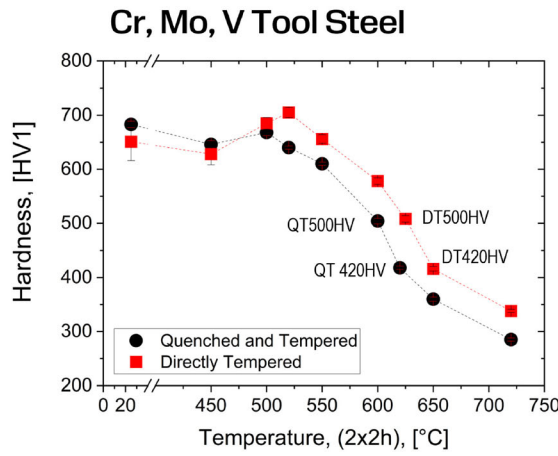
In laser additive manufacturing (AM) of hot work tool steels, direct tempering (DT) of the tool from as-built (AB) condition without prior conventional austenitization and quenching results in enhanced tempering resistance. To date, intercellular retained austenite (RA) decomposition, leading to a shift in secondary hardening peak temperature, and finer martensite substructure are reported to be responsible for such a behavior. In this work, authors aimed at studying the strengthening contributions by performing isothermal tempering tests for long times (up to 40 hours) at elevated temperatures (up to 650 °C) on DT and quenched and tempered (QT) specimens. The thermal softening kinetics and the microstructural evolution were evaluated with the support of computational thermodynamics. The results suggest that the main contributor to enhanced temper resistance in DT condition is the larger fraction of thermally stable and extremely fine (~ 20 nm) *secondary* (tempering) V(C,N) compared with QT. This could be explained by the reduction of available V and C in austenitized and quenched martensite for a later *secondary* V(C,N) precipitation during tempering, because of equilibrium precipitation of relatively large (up to 500 nm) vanadium-rich carbonitrides during the austenitization process. A complementary effect of the substructure refinement (*i.e.*, martensite block width) in rapidly solidified highly supersaturated martensite was also quantified in terms of Hall–Petch strengthening mechanism. The significant effect of *secondary* V(C,N) was successfully validated by assessing a laser AM processed vanadium-free hot work tool steel in QT and DT condition, where no significant differences in strength and temper resistance between the two conditions were evident.

FARAZ DEIRMINA is with the Sandvik Additive Manufacturing, Sandvik Machining Solutions AB, 811 80 Sandviken, Sweden. Contact e-mail: Faraz.deirmina@sandvik.com SASAN AMIRABDOLLAHIAN is with the Additive Manufacturing R&D, ProM Facility Area, Trentino Sviluppo S.p.A. Via Fortunato Zeni 8, 38068 Rovereto, Italy. GRETA LINDWALL is with the Department of Materials Science and Engineering, KTH Royal Institute of Technology, Brinellvägen 23, 100 44 Stockholm, Sweden. ALBERTO MOLINARI and MASSIMO PELLIZZARI are with the Department of Industrial Engineering, University of Trento, Via Sommarive 9, 38123 Trento, Italy. Contact e-mail: massimo.pellizzari@unitn.it JITENDAR KUMAR TIWARI and EDUARD HRYHA are with the Department of Industrial and Materials Science, Chalmers University of Technology, 412 96 Gothenburg, Sweden.
Manuscript submitted December 11, 2023; accepted September 25, 2024.
Article published online October 23, 2024

I. INTRODUCTION

AISI H13 is a Cr, Mo, V-alloyed hot work tool steel that is widely used in tooling applications due to its high hardness and strength, acceptable toughness, and resistance to thermal fatigue and wear at elevated temperatures.[1] Directed Laser Metal Deposition (DLMD), also known as Directed Energy Deposition (DED), is an additive manufacturing (AM) processing route getting growing attention thanks to the possibility to produce very complex parts in short time, and in a cost-effective way.[2,3] Possible applications of this technology are tools and dies with conformal cooling channels, and dies and molds repair, as well as production of multi-materials.[4–8] Indeed, H13 has been considered as one of the earliest alloys used in repairing dies using direct metal deposition back in 1990s in the pioneering work of Mazumder et al.[9] Despite the difficulties in processing H13 by laser-based DED (L-DED), due to residual stress accumulation resulting from martensitic transformation, numerous studies conducted in recent years demonstrate the successful deposition and characterization of L-DED H13 parts for tooling applications and repair.[4–8,10]

Hot work tool steels are generally austenitized and quenched and are finally tempered to the required hardness and toughness. Austenitization provides a nearly full dissolution of C and alloying elements inside the parent austenite. Quenching of the austenite below the martensite start temperature bypasses the diffusion-controlled reactions, and provides a highly supersaturated hard martensitic microstructure.[11,12] This is also true for substitutional alloying elements such as Cr, Mo, and Mn which are in supersaturation in the as-quenched BCC (BCT) structure of martensite.[13] Depending on the C, alloying content, and grains size, up to ~ 5 vol pct retained austenite (RA) can be expected in the quenched microstructure of H13.[14] The quenched martensite in H13 (~ 0.4 wt pct C) is characterized by high hardness due to lattice distortion, high dislocation density, C segregation to dislocations, and lath boundaries. In this condition, the quenched martensite shows a quite poor toughness. By tempering, or double tempering of the martensite above the secondary hardening temperature, i.e., by precipitation of secondary carbides, the toughness

of tempered martensite increases due to the reduction of lattice tetragonality, dislocation recovery, and depletion of carbon due to forming of alloy carbides.[13] In this condition, the material shows its optimum performance due to the good combination of properties such as hardness, toughness, abrasive wear, and thermal fatigue resistance.

In laser-based additive manufacturing such as powder bed fusion—laser beam (PBF-LB) and DED—the as-built (AB) H13 comprises a cellular/dendritic solidification structure, with heavy micro-segregation of carbon, and other alloying elements at the cellular boundaries. This results in a martensitic matrix, while the micro-segregated regions (i.e., intercellular/inter-dendritic areas) are characterized as RA (up to ~ 20 vol pct), and small volume fraction of carbides formed during the rapid solidification at the intercellular micro-segregation regions.[15–17] However, it has been suggested that in AM-H13, experiencing a fast cooling (e.g., 10^3–10^6 K/s) after laser deposition and following re-heating due to the melting of the layers above, AB microstructure can be potentially subjected to direct tempering and hence allowing to eliminate costly austenitization step.[15–20] The early works of various researchers in the field manifested a different tempering behavior of the AB and the quenched counterpart. It was agreed that, in directly tempered samples, decomposition of intercellular RA shifts the secondary hardening peak to higher temperatures and the tempered hardness was systematically higher than the quenched and tempered steel above the secondary hardness peak. This was explained considering; (i) more sluggish precipitation of secondary (tempering) carbides from the highly alloyed retained austenite (FCC) compared to that of martensite (BCT), and (ii) subsequent transformation of the low alloyed RA to fresh (hard) martensite during cooling from the tempering temperature.[15,17,18] Such a behavior was claimed to be promising because the component could be tempered at higher temperatures (i.e., + 25 °C) than those of quenched counterparts to achieve similar hardness levels. This potentially leads to an increased thermal stability. Indeed, in one of the few works on thermal fatigue behavior of AM H13, Pellizzari et al.[21] showed that even in short-term cyclic heating and cooling cycles, directly tempered H13 demonstrates an enhanced resistance to thermal softening. However, to date, and to the authors' best knowledge, there was no systematic study on long-term temper back resistance (i.e., softening behavior) of the directly tempered tool steel compared with those of quenched and tempered counterparts.

In this work, authors report on the peculiar microstructural response to long-time isothermal holding at elevated temperatures in directly tempered AISI H13 tool steel manufactured by L-DED. Furthermore, the mechanisms governing the thermal softening are discussed, with a focus on the effects of the elemental micro-segregation, martensite substructure size, secondary (tempering) carbide precipitation, and coarsening.

II. MATERIALS AND METHODS

Gas atomized AISI H13 powder from Sandvik Osprey® with a particle size distribution of − 109 μm + 57 μm was used as feedstock. Chemical composition is reported in Table I. C and N were measured by Leco analysis, and the rest of elements using inductively coupled plasma optical emission spectrometry (ICP-OES) in compliance with ISO/IEC 17025:2017. Trace and tramp elements including Al, Co, Hf, Nb, Ta, Ti, W, Pb, Sn, S, and P were all below 100 PPM, while Ni and O were measured to be 500 PPM and 230 PPM, respectively.

Cuboids of $45 \times 35 \times 10$ mm^3 were deposited on a C40 mild steel substrate, using a DMG MORI LASERTEC 65 3D hybrid machine with a Coax 14 powder nozzle. The machine has a diode laser ($\lambda = 1020$ nm), the spot diameter was 3 mm, with a top-hat beam profile and a focal length of 13 mm. Samples with relative densities of over 99.5 pct were obtained using laser deposition parameters of power (P) of 1400 W, powder flow rate of 12 g/min, and feed rate of 1 m/min using meander scanning strategy with 90 deg rotation between layers. High purity Argon was used as carrier and shielding gas with a flow rate of 5 L/min and 6 L/min, respectively. According to the previous work of the authors, these parameters resulted in a near fully dense microstructure.[22,23]

Moreover, in a previous work by the authors, it had been demonstrated that 1060 °C can be an optimum austenitization temperature for the L-DED H13 since it was possible to obtain partial homogenization of the micro-segregation while avoiding excessive grain growth.[16] This is in contrast with PBF-LB H13, where due to a finer cell size, lower vol pct, and much finer size of proeutectoid V-rich carbides in the as-built microstructure, homogenization and removal of the cellular solidification structure could be easily achieved by austenitization at lower temperatures (i.e., 1010 °C –1020 °C).[15,24] In this regard, for austenitized and quenched samples, austenitization at 1060 °C for 40 minutes followed by high pressure gas quenching was employed. Four different tempering scenarios, all above the secondary hardening peak temperature,[16] were selected to obtain two target hardness levels of ~ 500 HV1, and ~ 420 HV1 for both "quenched and tempered" (herein after QT), and "directly tempered" (herein after DT) condition. These hardness levels are often recommended for the H13 tool steel in its intended applications (e.g., aluminum alloys high pressure die casting dies, tool holders, forging, and extrusion dies). Tempering resistance of the L-DED samples was evaluated by placing 2 sets of QT and DT samples

Table I. Feedstock Powder Chemical Composition, in Weight Percent

C	Cr	Mo	V	Si	Mn	N	Fe
0.40	5.10	1.58	1.0	0.95	0.30	0.05	bal.

Table II.   Summary of Specimen Description and Codes

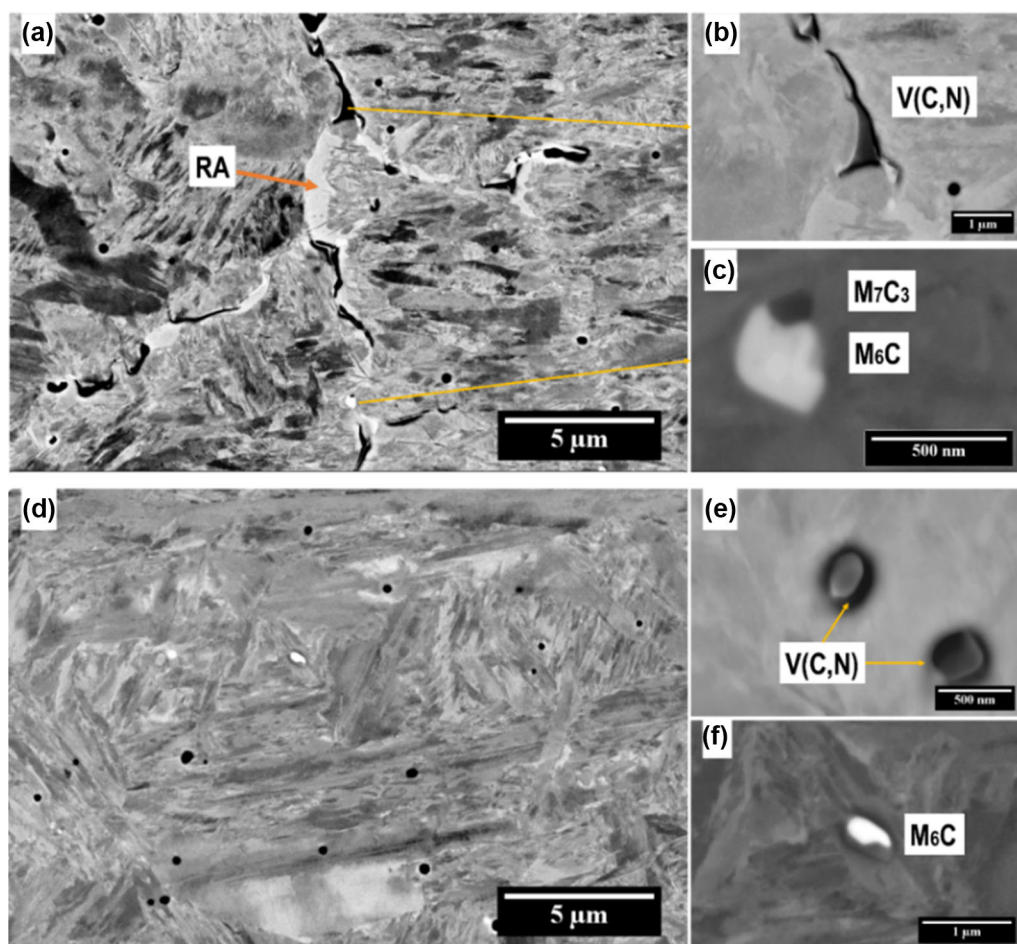| Code	Description	Austenitized, and Quenched	Tempering Temperature (2×,2 h), [°C]	Hardness, [HV1]
AB	as-built specimen	No	—	651 ± 35
Q	quenched specimen	Yes	—	630 ± 5
DT500HV	directly tempered from AB condition	No	625	500 ± 6
QT500HV	quenched and tempered	Yes	600	508 ± 14
DT420HV	directly tempered from AB condition	No	650	418 ± 7
QT420HV	quenched and tempered	Yes	620	420 ± 3

Fig. 1—BSE micrographs of (a) AB H13, (b) intercellular V(C,N), (c) intercellular M_6C-M_7C_3, (d) austenitized and quenched (Q) H13, (e) V(C,N) precipitated during austenitization, and (f) undissolved M_6C. Adapted from Ref. [16].

(micro-cut to 15 × 15 × 10 mm^3) in a muffle furnace at 600 °C and 650 °C, under protective Ar atmosphere. Hardness of the specimens was measured after soaking times of 1, 5, 20, and 40 hours. Table II summarizes the samples and respective heat treatments.

Metallographic cross-sections were prepared by grinding up to 1200 grit, subsequent polishing with 3 μm and 1 μm diamond pastes, followed by a final oxide polishing (colloidal silica suspension 0.02 μm). Microstructural characterizations were conducted on metallographic cross-sections using Field Emission Gun Scanning Electron Microscopy (FE-SEM, Zeiss Sigma, Germany). For the image analysis, ImageJ open software was used. Electron backscattered diffraction (EBSD) combined with electron dispersive x-ray spectroscopy (EDS) elemental mapping was performed using a Symmetry EBSD detector on FE-SEM. SEM imaging and EDS spot analysis were performed using an accelerating voltage of 10 kV, and 20 kV was used for the EBSD analysis, and the post processing of EBSD
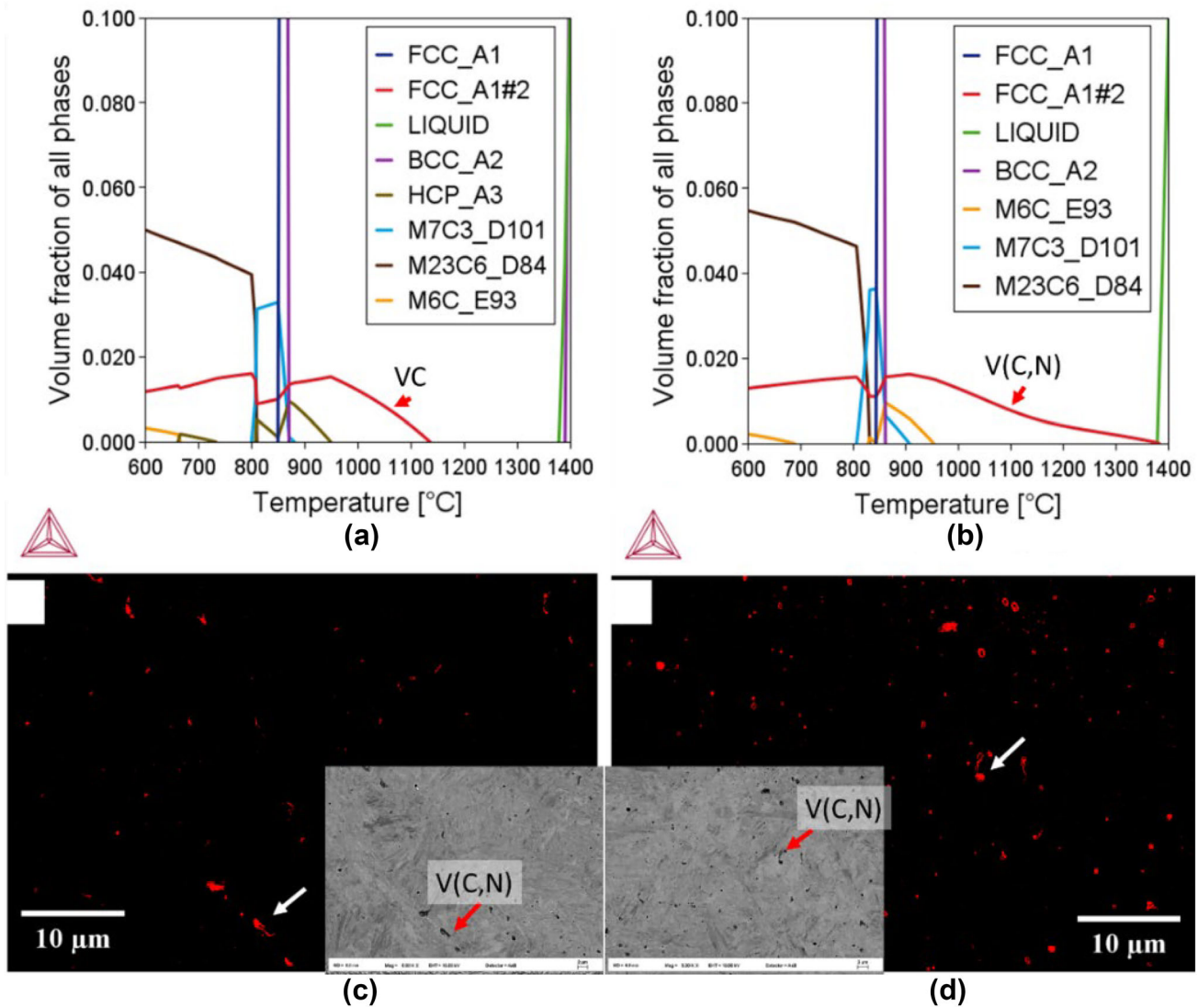
Fig. 2—Equilibrium diagrams displaying the volume fraction of phases in H13 (*a*) without N, and (*b*) with 500 ppm N; image analysis results on the area fraction of V(C,N)- red in binary images (*c*) AB H13, and (*d*) Q H13 (Color figure online).

results was conducted using Channel 5 suite (Tango mapping). For the geometrically necessary dislocations (GNDs) density measurements using EBSD results, the procedure in the work of Konijnenberg *et al.*[25] in calculating the GNDs density of martensite was followed. Transmission electron microscopy (TEM) was conducted to characterize nanosized tempering carbides. For this purpose, a rectangular slice of dimensions 200 μm × 10 mm × 10 mm was cut from the sample using slow speed cutting to avoid any deformation and heating of the sample. This slice was further thinned down up to 80 μm using 2000 grit emery paper. The thin slice was cleaned with ethanol and punched to extract 3 mm disks. These disks were further electropolished to achieve electron transparent region by using a twin jet polisher (Struers) at 10 V and—30 °C in10:90 perchloric acid and methanol electrolyte. The prepared samples were examined under TEM, (FEI Technai T 20 LaB6, 200 kV). Hardness (HV1) measurements were performed according to ASTM E92-17 using a FM310
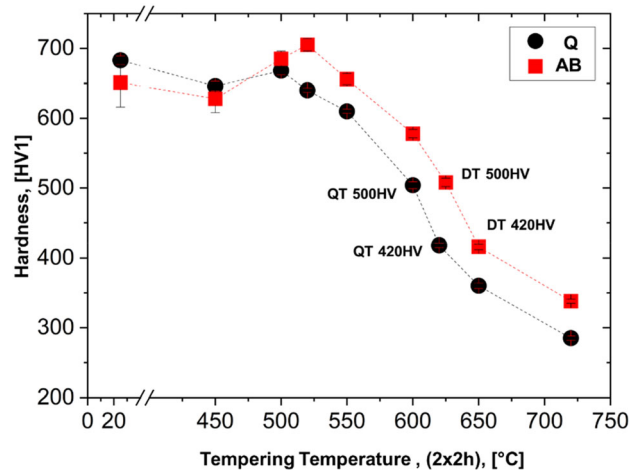

Fig 3—Tempering curves of AB and Q H13 for 2 × 2 h tempering, samples selected for long-time temper resistance tests are marked in the figure, Adapted from Ref. [16].

equipment (FUTURE-TECH CORP., Japan) with a loading time of 10 seconds. Thermo-calc software (TCFE11, MOBFE6)[26] was used for the calculations of equilibrium diagrams and solidification modeling. For the latter, to better elaborate on the diffusion of elements during the rapid solidification process, DICTRA simulations were applied. Using DICTRA, the liquid/solid phase transformation in one dimension can be solved under the assumptions of a sharp interphase boundary, where local equilibrium holds at the interface. To perform the simulations, cooling rate of ~ 2000 K/s was used based on the previous work of the authors where the cooling rates during the process were successfully simulated and experimentally validated,[27] moreover, a simulation domain size of 2.5 μm corresponding to the average radius of the cellular solidification structure in the current samples was considered.

III. RESULTS

A. *Recap on As Built and Quenched Microstructure and Phases*

A recap from the previous work of the authors is shown in SEM micrographs in Figure 1, obtained with backscatter mode (BSE).[16] The microstructure of the AB-H13 is composed of a martensitic matrix, with the presence of RA at the cellular/dendritic boundaries [Figure 1(a)]. Cell boundaries are also characterized by the isolated, and relatively large (1 to 2 μm) V(C,N) stringers, M_6C, and M_7C_3 type proeutectoid carbides precipitated during the solidification because of the local enrichment (*i.e.*, micro-segregation) of the carbide forming alloying elements [Figures 1(b) and (c)].[16] In the Q microstructure, there are no traces of RA, and the cellular structure is removed by the formation of new austenite grains during high-temperature austenitization [Figure 1(d)].[16] Newly precipitated stable annealing V(C,N) or V_2(C,N),[28] up to 500 nm in size, with a different morphology compared with those of AB (*i.e.*, finer particles *vs.* stringers) could be found in the

Fig. 4—Hardness *vs.* Tempering parameter (T_p), for up to 40 h over-tempering.

microstructure. Moreover, some undissolved M_6C carbides were still present [Figures 1(e), and (f)].[16]

The stability of existing V(C,N) carbides and the precipitation of new ones during austenitization can be explained by thermodynamic calculations. VC is an equilibrium phase at 1060 °C, *i.e.*, the austenitization temperature used in this work [Figure 2(a)]. Other carbide types are not, so that their dissolution occurs during austenitization. Indeed, the presence of nitrogen even extends the stability of V(C,N) to higher temperatures, and it is plausible that the nitrogen content of the powders, as well as the nitrogen pick-up during the L-DED process,[16] results in the formation of more thermally stable V(C,N). This is shown in equilibrium diagram, considering 500 ppm of N (see Table I) [Figure 2(b)]. Furthermore, by incorporation of nitrogen, the stability of V (C, N) is extended to above solidus temperature, a good qualitative indication of the presence of coarse V (C, N) stringers at the cell boundaries of the rapidly solidified steel. The calculations suggest that ~ 0.98 vol pct V(C,N) (FCC_A1#2) is stable at 1060 °C, accordingly the matrix (austenite FCC_A1) is depleted by a maximum of ~ 0.55 wt pct V, and ~ 0.08 wt pct C as a result of V(C,N) formation under equilibrium condition. Figures 2(c), and (d) show an image analysis on BSE micrographs at 5kX magnification, confirming the lower vol pct of V(C,N) in AB (0.32 pct) compared with Q H13 (0.71 pct).

Tempering curves [Figure (3)] highlight a different tempering behavior for DT and QT. The starting hardness of the Q material is higher than that of AB mainly because of removing softer RA (*i.e.*, 12 vol pct in AB condition[16]) after austenitization and quenching. In agreement with the previous studies,[15–18] the secondary hardening peak in DT is shifted to higher temperatures compared with QT (*i.e.*, 520 °C *vs.* 500 °C). This shift was attributed to the decomposition of RA, producing carbides and fresh martensite during the first tempering cycle especially by tempering at temperature higher than 500 °C, as discussed in detail in the previous work of authors using dilatometry studies,[16] as well as that of Fonseca *et al.*[29] using high-temperature synchrotron X-ray diffraction. The tempered hardness in DT samples at temperatures higher than the secondary hardening peak is always systematically higher than that of QT, showing a relatively constant hardness difference of ~ 50 HV1, which was ascribed to the effect of RA decomposition and finer martensite substructure size of DT samples as a result of rapid solidification.[15–18,29] The samples highlighted in Figure 3 were used for thermal softening resistance tests through isothermal soaking by up to 40 hours either at 600 °C, or 650 °C, as described in Section III–B. As evident, both pairs of samples (DT500HV, QT500HV) and (DT420HV, QT420HV), having the same starting hardness (*i.e.*, ~ 500 HV1, and ~ 420 HV1, respectively), are tempered well above the secondary hardening temperature (see Figure 3), where any RA is completely removed.[15–17] So, any strengthening contribution from metastable RA decomposition in DT samples during the long-term tempering resistance tests should be disregarded.
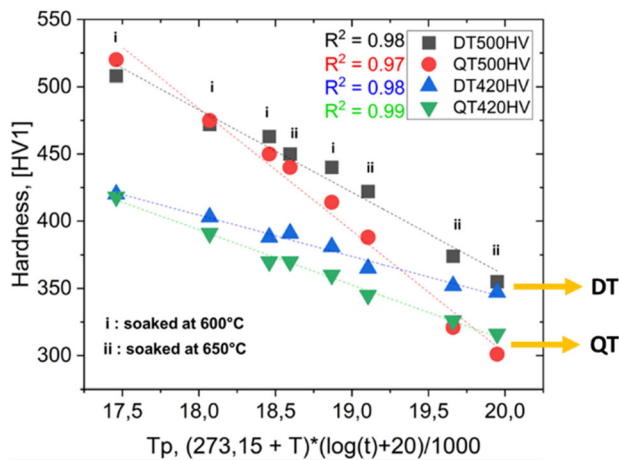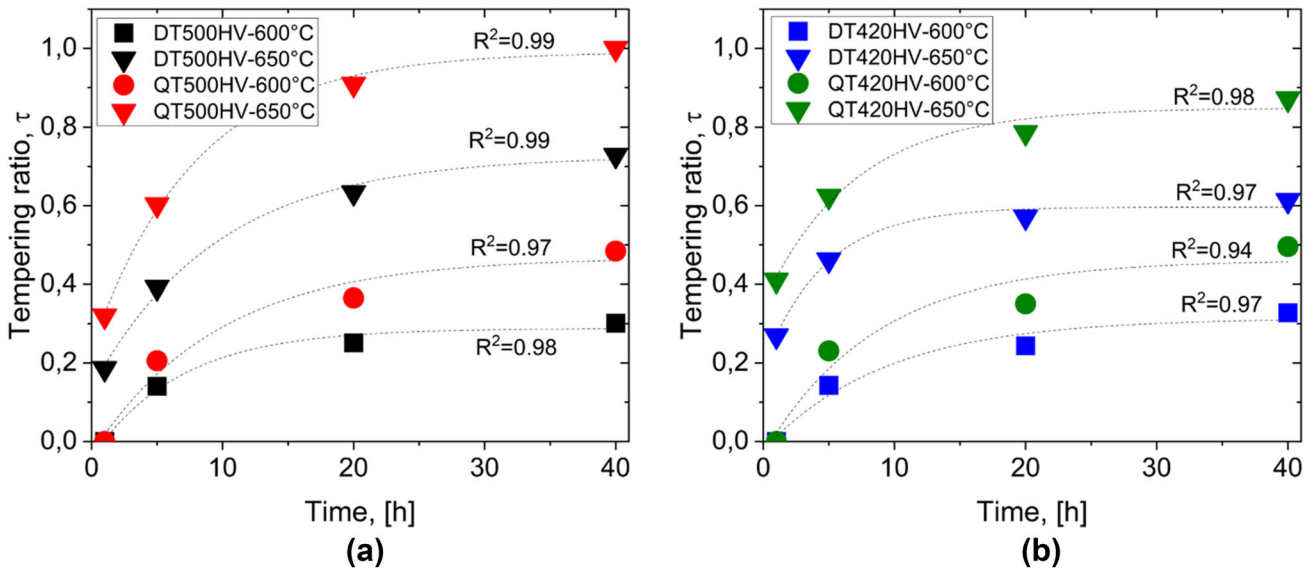
Fig. 5—Tempering ratio *vs.* soaking time (*a*) DT500HV and QT500HV soaked at 600 °C and 650 °C, (*b*) DT420HV and QT420HV soaked at 600 °C and 650 °C.

B. *Tempering Resistance*

The hardness results for long-term tempering are depicted against the tempering parameter (T_p), also known as the Hollomon–Jaffe parameter or the Larson–Miller parameter, where $T_p = (273.15 + T) \times ($ log(t) + 20)/1000, where T is the tempering temperature in degrees Celsius, and t is the tempering time, in hours (Figure 4). The raw data and the standard deviations (1σ) are added to electronic supplementary Table S1. Data points are marked as (i) for 600 °C, and (ii) for 650 °C holding temperatures. Looking at the slope of the fitted lines, it is evident that at similar starting hardness, DT samples still show a statistically significant higher tempering resistance compared to their QT counterparts, and this difference becomes larger by increasing the soaking time (*i.e.*, QT and DT tend to diverge). As an example, for DT500HV and QT500HV, after 40 hours holding at 650 °C, the hardness drops from ~ 500 HV1 to ~ 350 HV1, and 301 HV1, respectively. This condition holds for DT420HV and QT420HV yielding hardness of 347 HV1, and 316 HV1 respectively, under the same testing condition. One might argue that QT samples were initially tempered at a lower temperature compared with DT counterparts to achieve similar starting hardness (see Table II, and Figure 3) which might increase their softening kinetics during the long-time tempering tests at 600 °C and 650 °C. While this might be true for the early stages of soaking, but as clearly shown in Figure 4, regardless of the initial tempering temperature and hardness, both QT specimens (*i.e.*, QT500HV and QT420HV) show an equal final hardness of ~ 300 HV1 after 40 h soaking at 650 °C, meaning that the softening after a very long-time soaking at this temperature was independent of initial tempering temperature. This behavior is indeed similar for the DT samples, where both samples show a hardness of ~ 350 HV1 at the end of the tests.

Therefore, the important observation is the markedly higher softening resistance of DT samples even at long soaking times at relatively high tempering temperatures, where significant over-tempering is expected.

C. *Thermal Softening Kinetics*

In order to elaborate on the improved temper resistance behavior of the DT samples, firstly the concept of tempering ratio, a kinetics law based on hardness was used to calculate the softening kinetics and the activation energy for thermal softening.[30] For this purpose, Eq. [1] was applied.

$$\tau = \frac{H - H_0}{H_\infty - H_0}, \quad [1]$$

where τ is the tempering ratio, H is the measured hardness of the part after a certain tempering time, H_0 is the starting hardness (*e.g.*, normally taken as quenched hardness), and H_∞ is the hardness in fully over-tempered (soft) condition. However, in this experiment, as the softening resistance after double tempering was the main objective, and due to the comparative nature of Eq. [1], H_0 was set to 420 HV1 and 500 HV1, respectively, for the 2 pairs of samples corresponding to their starting hardness. Accordingly, H_∞ was set to the minimum hardness recorded after completion of the tests, *i.e.*, 301 HV1 after 40 hours over-tempering at 650 °C, very close to the hardness of H13 in fully annealed condition (*i.e.*, ~ 250 HV).[31] Tempering ratio calculations of the mean hardness evolution over time for DT & QT-500HV and DT & QT-420HV are shown in Figure 5a and b, respectively. Seemingly the tempering ratio is an exponential function of the tempering time for both tempering conditions (*i.e.*, DT and QT) and both tempering temperatures (*i.e.*, 600 °C, and 650 °C), always representing faster softening for the QT
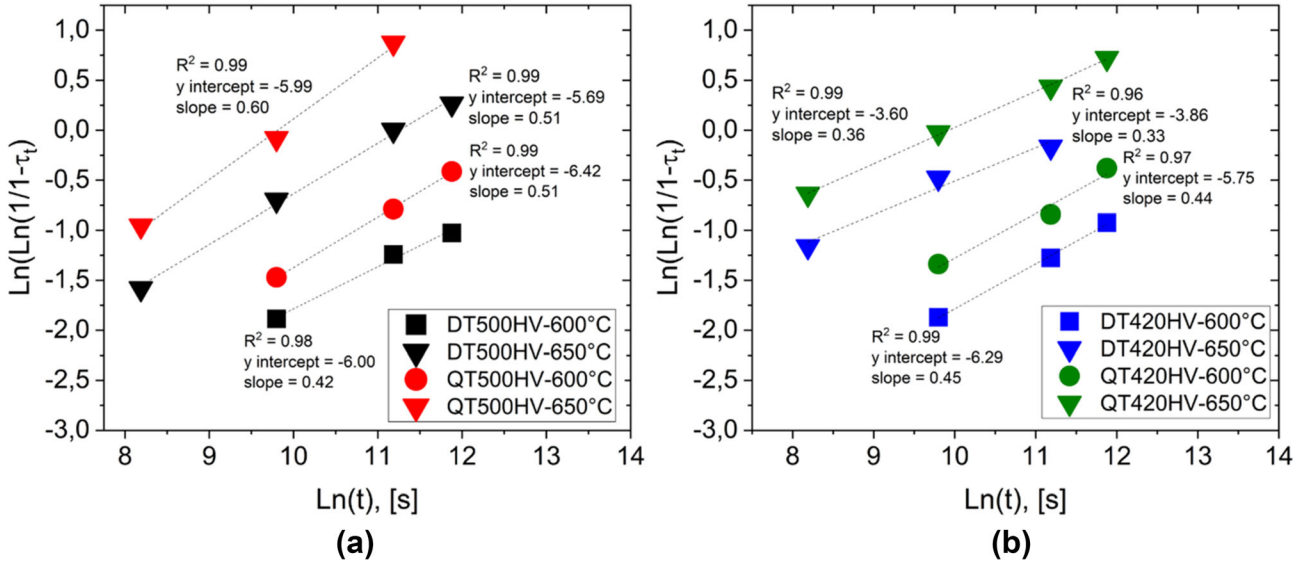
Fig. 6—Ln(Ln($\frac{1}{1-\tau_t}$)) vs. Ln(t), the slope and Y-intercept of the fitted lines: (*a*) DT500HV and QT500HV soaked at 600 °C and 650 °C, (*b*) DT420HV and QT420HV soaked at 600 °C and 650 °C, note i is in seconds.

Table III. Avrami Exponent and Activation Energies of Softening at Two Different Holding Temperatures

Sample	Initial Tempering Temperature (°C)	Holding Temperature Up to 40 h (°C)	Avrami Exponent (*n*)	Ln(*D*)	Activation Energy (Q)kJ/mol
DT500HV	625	600	0.42	− 6.0	230
DT500HV	625	650	0.51	− 5.7	240
QT500HV	600	600	0.50	− 6.4	233
QT500HV	600	650	0.60	− 6.0	243
DT420HV	650	600	0.45	− 6.3	232
DT420HV	650	650	0.33	− 3.9	227
QT420HV	620	600	0.44	− 5.7	228
QT420HV	620	650	0.36	− 3.6	225

specimens. The data and corresponding standard deviations of tempering ratio measurements are added to electronic supplementary Table S2.

Indeed, thermal softening can be ascribed to solid-state transformations governed by diffusion, as confirmed by the tempering ratio which shows an exponential behavior against time.[32] Therefore, referring to literature, it is convenient to formulate the tempering kinetic law in the form of Johnson–Mehl–Avrami–Kolmogorov (JMAK) equation as follows,[32,33]

$$\tau = 1 - e^{(-Dt^n)}, \quad [2]$$

where t is the tempering time, n is Avrami exponent that is dependent on the material previous thermal history, D is dependent on the tempering temperature, and can be written in the form of Arrhenius equation:

$$D = D_0 e^{(\frac{-Q}{RT})}, \quad [3]$$

where D_0 is a pre-exponential constant, Q is the activation energy of the tempering transformation, R is the

gas constant (*i.e.*, 8.3143 kJ mol^{-1} K^{-1}), and T is the isothermal tempering temperature in Kelvin.

Here, Eq. [2] can be written as a function of ln(t), and ln (ln (1/(1−τ)) as follows:

$$Ln\left(Ln\left(\frac{1}{1-\tau}\right)\right) = nLn(t) + LnD. \quad [4]$$

Plotting the left side of the Eq. [4], against Ln(t), allows to determine the Avrami exponent (*n*) as the slope of the linear regression fit, while Ln(*D*) could be derived as the Y-intercept of the fitted lines according to Eq. [4]. This is shown in Figures 6(a) and (b).

The Avrami exponents (Table III) are lower in samples initially tempered at higher temperatures. Avrami exponents close to 0.5 were claimed to be ascribed to a mechanism after which carbides nuclei form at dislocations/lath boundaries and block boundaries, whose growth is controlled by the diffusion of the carbide forming elements (*i.e.*, Cr, Mo, and V).[32,34] Lower *n* values are reported in case of dislocation recovery of the lath martensite at higher temperature
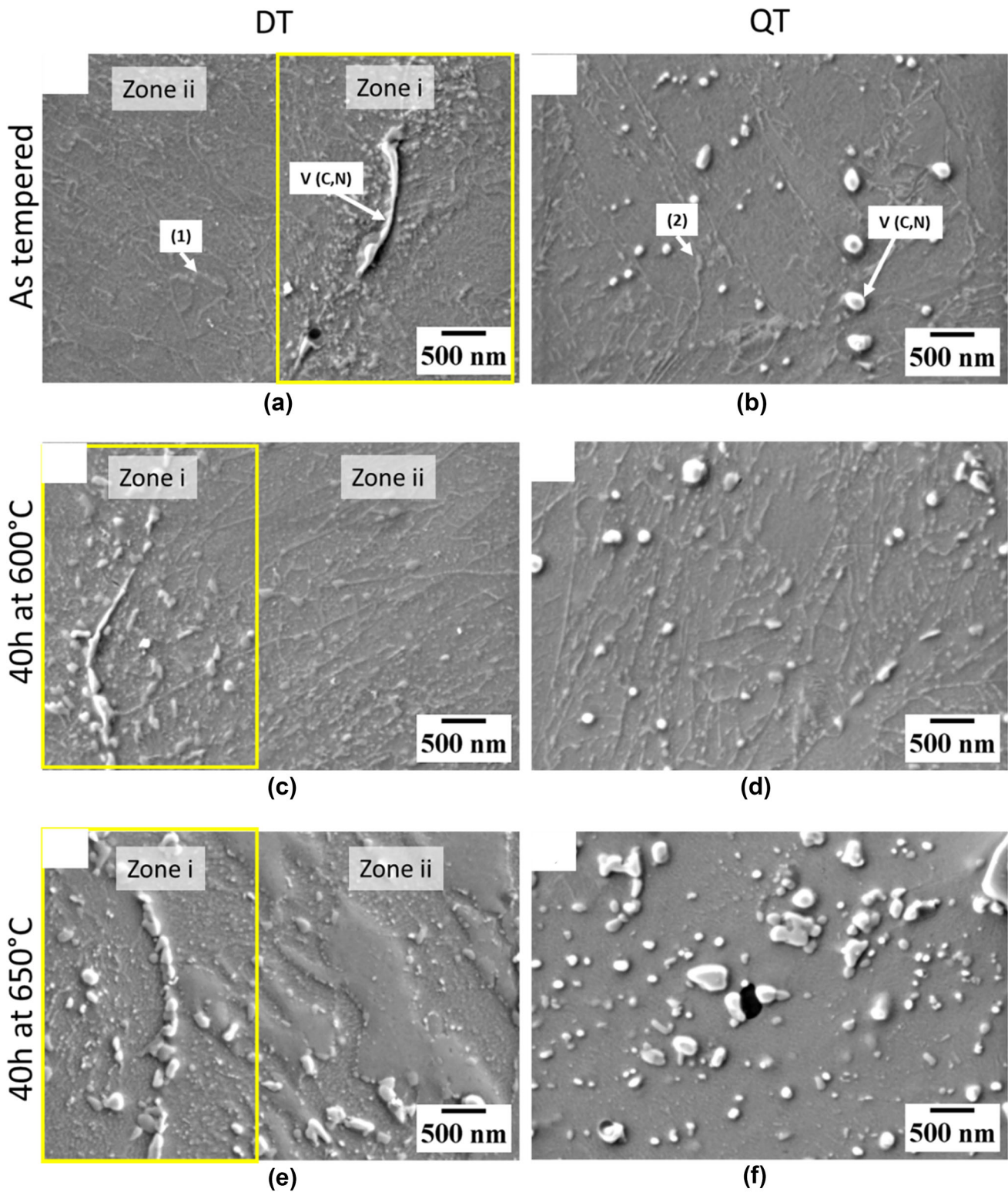
Fig. 7—Secondary electron (SE) micrographs of (*a*) as-tempered DT500HV, (*b*) as-tempered QT500HV, (*c*) DT over-tempering (40 h, 600 °C), (*d*) QT over-tempering (40 h, 600 °C), (*e*) DT over-tempering (40 h, 650 °C), and (*f*) QT over-tempering (40 h, 650 °C).

tempering.[32,34] By knowing *n* and *D* from Figure 6, and using literature value (*i.e.*, $1.45 \times 10^{11} \text{s}^{-1}$[34]) for the pre-exponential constant D_0, the activation energy for the transformations causing softening could be calculated from Eq. [3] (reported in Table III). The activation energies for the initially harder samples (*i.e.*, 500 HV1) were in the range of 230 to 240 kJ/mol, while the activation energies for the initially softer samples (*i.e.*, 420 HV1) tempered at higher temperatures were in the range of 225 to 230 kJ/mol. Firstly, the values obtained

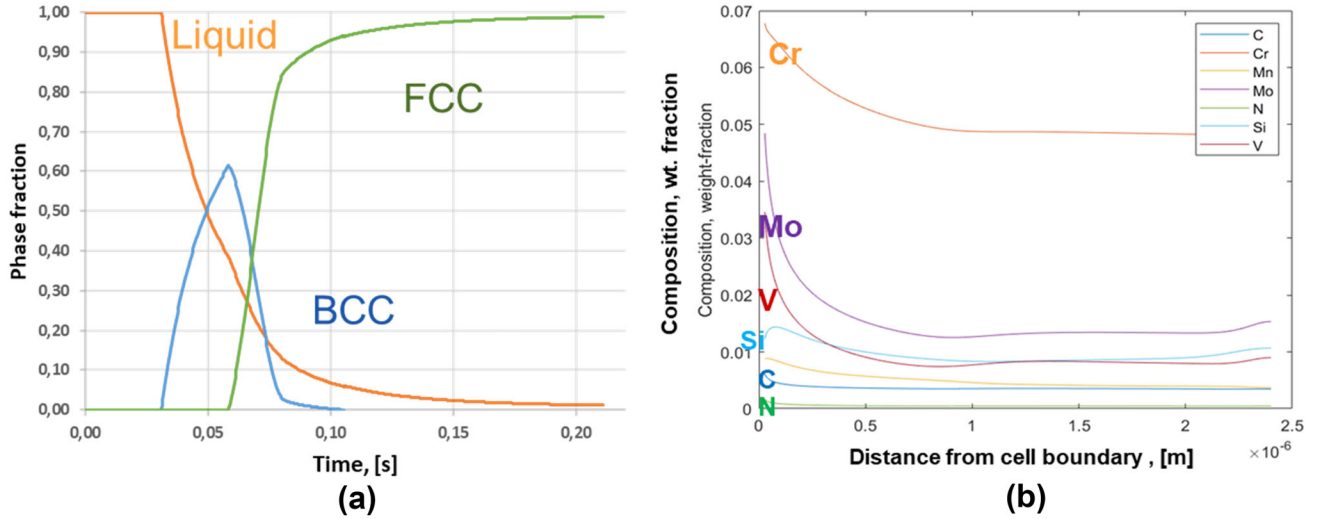| Sample	Cr	Mo	V	Si	Mn	N	Fe
V (C, N) DT	10.3 ± 0.5	7.6 ± 0.4	31.5 ± 0.6	0.9 ± 0.1	—	5.5 ± 0.4	bal.
V (C, N) QT	8.3 ± 0.6	4.3 ± 0.5	23.1 ± 0.7	1.0 ± 0.1	—	5.0 ± 0.3	bal.
Point 1	16.0 ± 3.2	6.0 ± 3.1	2.2 ± 1.2	1.0 ± 0.2	1.3 ± 0.7	—	bal.
Point 2	36.5 ± 1.3	4.0 ± 0.7	2.8 ± 0.5	1.0 ± 0.2	—	—	bal.
Matrix	5.3 ± 0.1	1.8 ± 0.1	1.1 ± 0.1	0.9 ± 0.1	0.6 ± 0.3	—	bal.

Fig. 8—(a) Dictra solidification simulations considering a cooling rate of 2×10^3 K/s: phase fraction *vs.* solidification time, (b) micro-segregation profiles from cell center to the cell boundary, as a function of distance from cell boundary (cell size is 5 μm).

are close to activation energies for the bulk diffusion of Cr (~ 250 kJ/mol), Mo (~ 240 kJ/mol), and V (~220–240 kJ/mol) in ferrite,[30,33,35,36] while for the initially softer samples over-tempered at higher temperatures, the values are closer to that of vanadium. This indicates that at high temperatures and long holding times, strengthening is governed by the coarsening of secondary (tempering) MC-type V-rich carbides (carbonitrides).[37] Secondly, the values evidence that the softening mechanism is similar in the samples. Therefore, the enhanced softening resistance in DT samples at long holding times should be a consequence of the microstructural features affiliated with rapid solidification, enhancing the strength of the over-tempered microstructure.

D. Microstructure and Phases in Over-Tempered Condition

Microstructures of DT500HV and QT500HV specimens in the as-tempered and over-tempered conditions of 600 °C, 40 hours, and 650 °C, 40 hours are shown in Figure 7. Microstructure in the as-tempered DT samples can be divided into two zones, *i.e.*, cell boundaries identified by stringers of V(C,N), and cell-core or matrix, as shown in Figure 7(a) and Table IV. Colonies

of finer secondary (tempering) carbides are evident at the vicinity of intercellular V(C,N). On the other hand, QT comprises a more uniform microstructure [Figure 7(b)]. In QT steel, additional globular V(C,N)/ V_2(C,N) are present [Figure 7(b), and Table IV]. As discussed previously, these carbonitrides precipitate during the austenitization process. In both conditions, indications of fine Cr-rich carbides precipitated on the block boundaries are evident [marked by 1 and 2 in Figures. 7(a) and (b), and Table IV] A more detailed characterization of these carbides will be presented later coupled with EBSD results.

In over-tempered DT samples [Figure 7(c), *soaked for 40 hours at 600 °C*)], a coarser secondary (tempering) carbides distribution near the prior cellular boundaries at the vicinity of V(C,N) is evident. This can be realized by comparing zones i (*i.e.*, near intercellular regions) and ii (*i.e.*, cell center) in both Figures 7a and c. QT shows a more homogeneous distribution of secondary (tempering) carbides with obvious coarsening, especially at the block and lath boundaries [compare Figures 7(b) and (d)]. After soaking at *650 °C for 40 hours*, a much coarser substructure is evident in both samples [Figures7(e) and (f)]. This confirms the occurrence of dislocation recovery, partial recrystallization in martensite substructure and coarsening, kinetically activated at
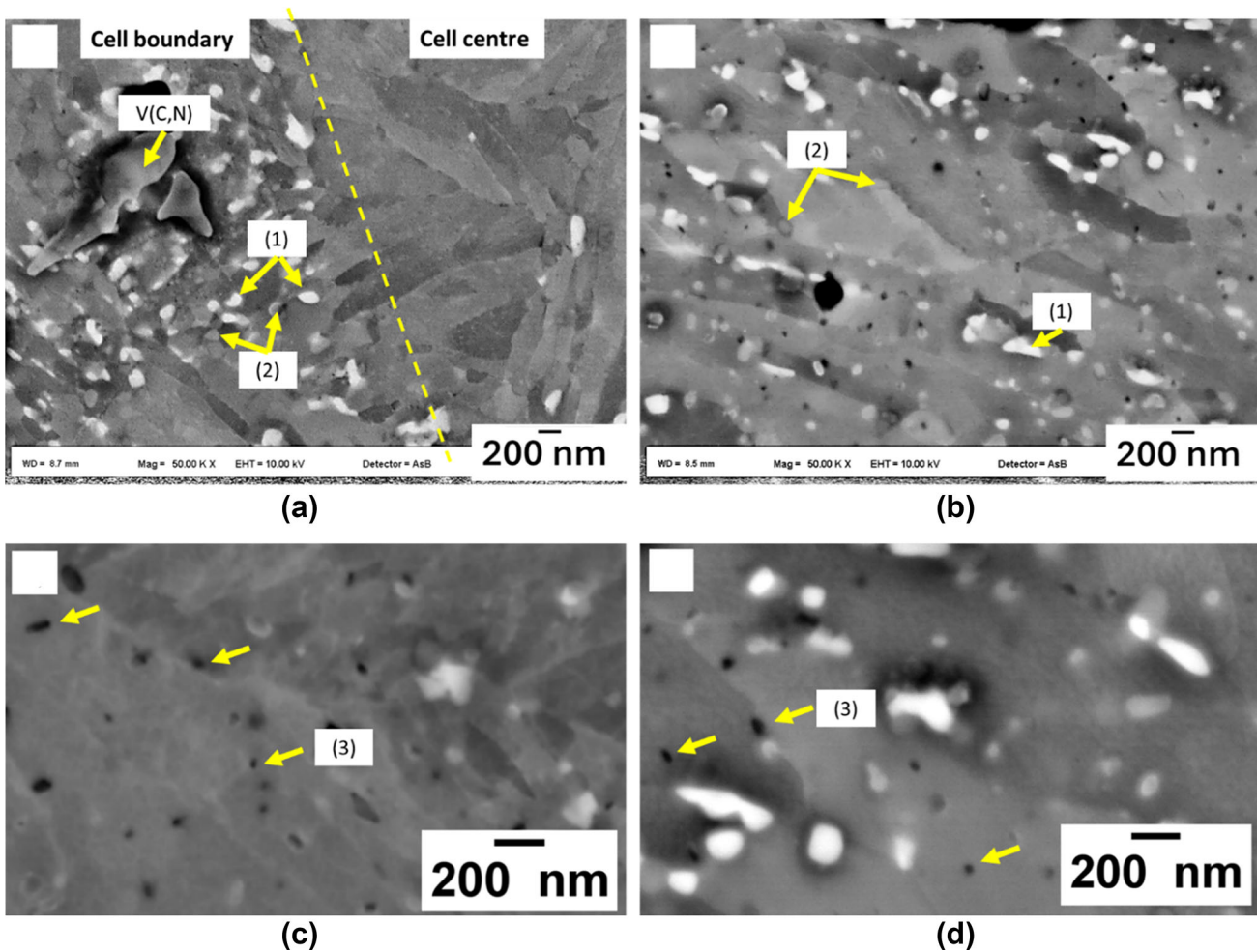
Fig. 9—BSE micrographs of over-tempered samples (40 h, 650 °C): (*a*) DT, (*b*) QT, (*c*) higher magnification (100 kX) showing secondary (tempering) V(C,N) in DT, and (*d*) higher magnification (100 kX), showing secondary (tempering) V(C,N) in QT.

650 °C.[13,34] The carbides in both samples became coarser. The secondary (tempering) carbide size near the cell boundaries of DT is slightly larger than the QT carbides, while the ones in the cell center (matrix) seem to be finer than that of QT.

Carbide coarsening at the intercellular regions can be explained in view of the heavy micro-segregation of alloying elements and C to the cell boundaries during the solidification as shown by DICTRA (Thermo-calc) simulations considering the cooling rates of ~ 2.0×10^3 K/s from previous work of the authors,[38] and a cell size of 5 μm [see Figures 8(a) and (b)]. As depicted in Figure 8(a), a solidification mode of primary δ-ferrite was considered. König *et al.*[38] showed that at cooling rates below 2.12×10^4 K/s, δ-ferrite is the primary phase to form in H13, followed by austenite formation. In Figure 8(b), the corresponding solid phase composition at the end of solidification (*i.e.*, 98 pct of liquid solidified) is shown as a function of distance from the cellular boundaries to the core of the cell. The micro-segregation of the alloying elements toward the intercellular area is evident. Consequently, the thermodynamic driving force for carbide precipitation from martensite (ferrite) in those regions increases as

confirmed in FEG-SEM images in Figure 7, and later will be shown more appropriately in connection with coupled EBSD-EDS mapping results.

In order to elaborate on the improved tempering resistance of DT samples, the extreme condition was selected (*i.e.,* DT500HV and QT500HV samples soaked for 40 hours at 650 °C). As a remark, in this condition, DT hardness was ~ 350 HV1 ,while QT showed ~ 300 HV1. In both cases, at least 3 types of secondary (tempering) carbides were identified. Thanks to carbide coarsening after 40 hours of exposure to 650 °C, EDS analysis using 10 kV accelerating voltage, and 10 to 15 seconds exposure time, characterized by a smaller beam interaction volume with the matrix, could give a reliable yet semi-quantitative analysis of these carbides. BSE micrographs shown in Figures 9(a) through (d) together with EDS point analysis helped to distinguish these carbides. The secondary (tempering) carbides detected in both alloys were Mo-rich carbides (points 1-brighter than the matrix in BSE mode) with sizes of ~ 70 to 250 nm, Cr-rich carbides, usually found on the martensite substructure boundaries (points 2- gray in BSE mode), with sizes of ~ 50 to 150 nm, and finally very fine and stable *secondary* (tempering) V(C,N)

Table V. EDS Spot Analysis Results on Points Marked in Fig. 9, in Weight Percent, (95 Percent Confidence)

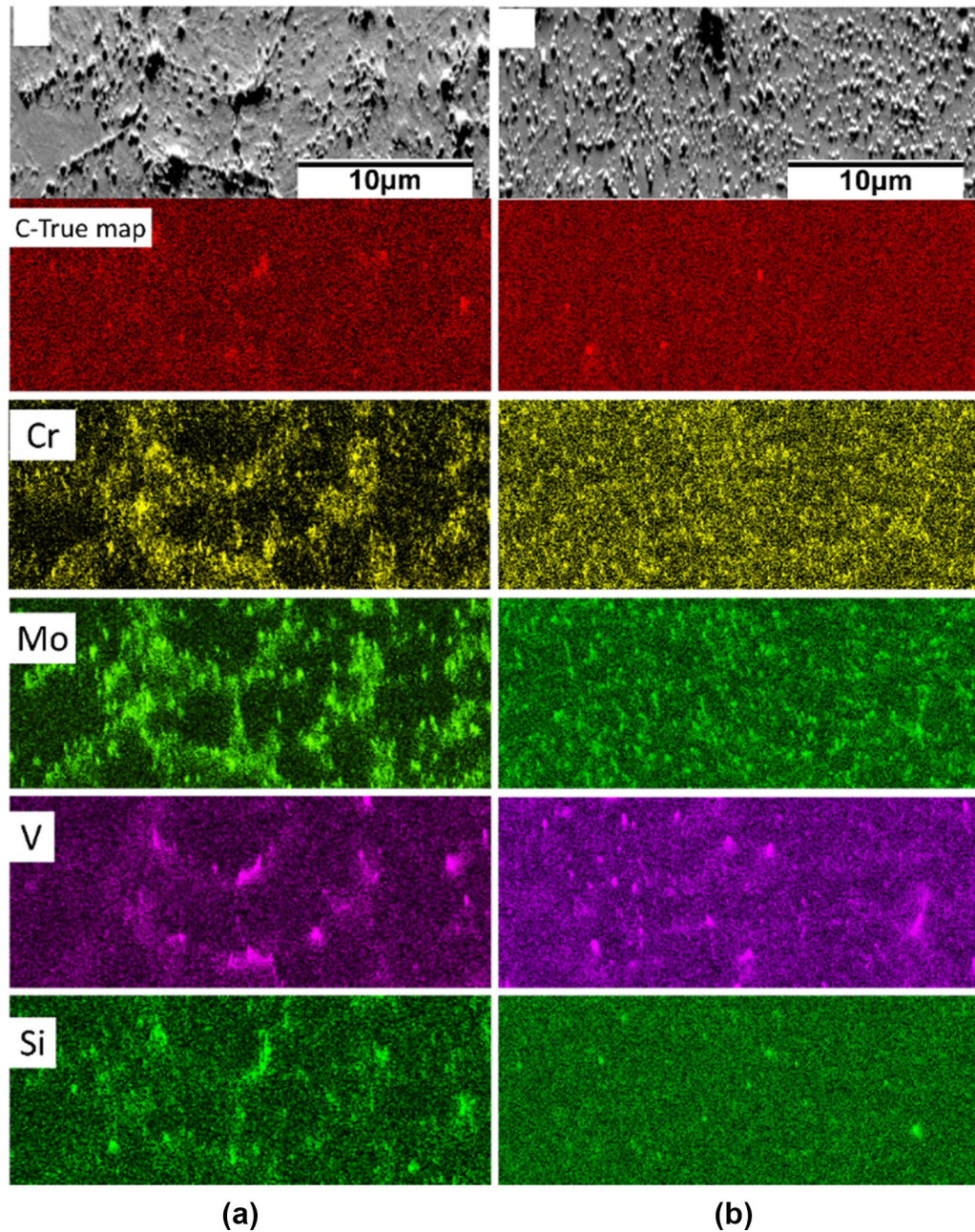|	Cr	Mo	V	Si	Mn	N	Fe
DT-1	9.5 ± 0.4	18.0 ± 0.6	2.7 ± 0.3	2.7 ± 0.1	—	—	bal.
QT-1	8.1 ± 0.4	17.4 ± 0.5	2.5 ± 0.3	2.5 ± 0.1	—	—	bal.
DT-2	16.5 ± 0.5	7.5 ± 0.3	1.9 ± 0.2	1.0 ± 0.1	1.3 ± 0.3	—	bal.
QT-2	18.7 ± 0.7	3.3 ± 0.4	1.7 ± 0.4	0.8 ± 0.1	—	—	bal.
DT-3 secondary V(C,N)	9.0 ± 0.5	5.6 ± 0.4	24.0 ± 0.6	0.7 ± 0.3	0.2 ± 0.1	3.2 ± 0.3	bal.
QT-3 secondary V(C,N)	9.5 ± 0.6	3.6 ± 0.4	16.7 ± 0.6	0.9 ± 0.1	—	1.7 ± 0.2	bal.

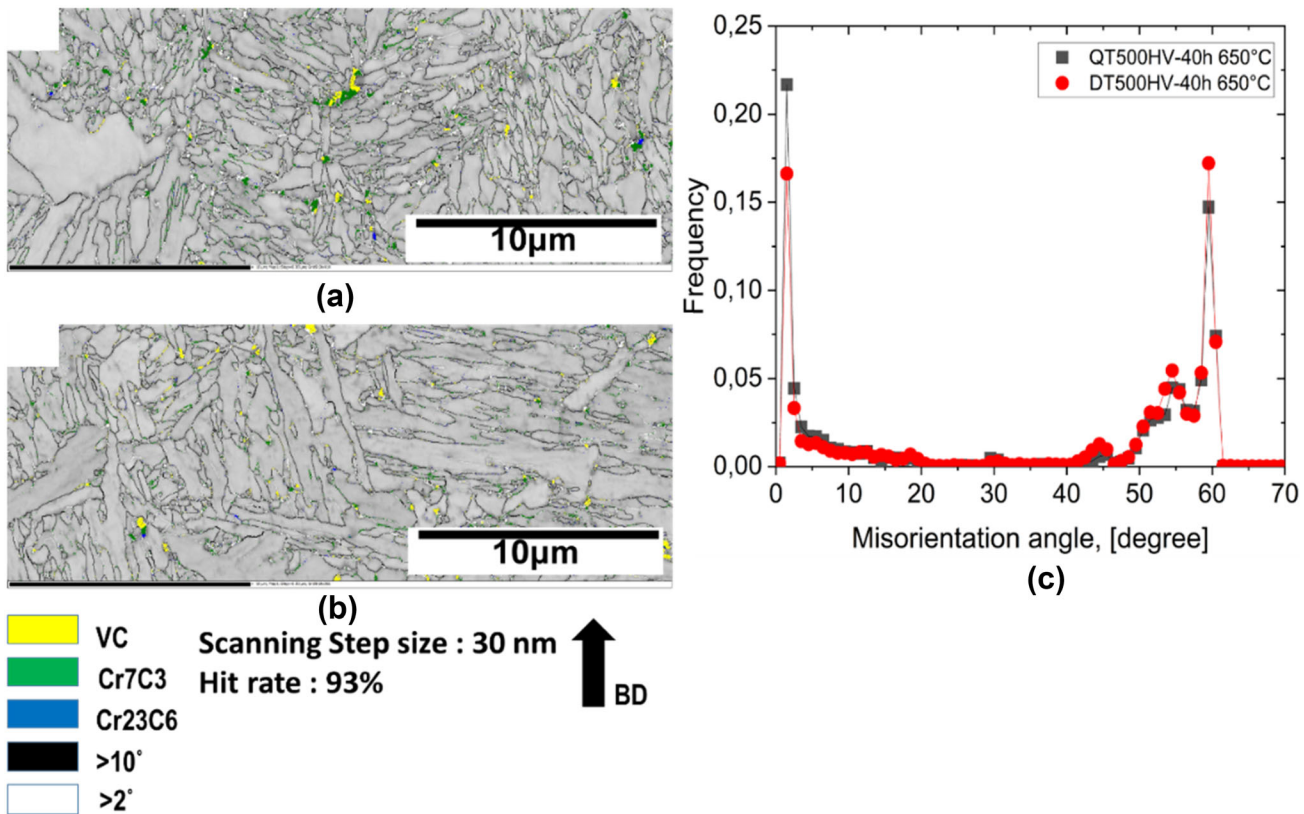Fig. 10—EDS elemental mappings for samples soaked for 40 h at 650 °C, (*a*) DT500HV, and (*b*) QT500HV.

Fig. 11—BC maps overlaid by boundaries with misorientation angles of > 2 deg, and > 10 deg, and carbide phase maps in samples soaked for 40 h at 650 °C (*a*) DT500HV, (*b*) QT500HV, and (*c*) misorientation angle distributions.

(points 3—darker than the matrix in BSE mode). It is possible to distinguish between the size of secondary (tempering) V(C,N), less than 40 nm in size, and those of coarse V(C,N) formed either during solidification (proeutectoid carbides, stringer like shapes) or austenitization (stable annealing carbides, globular) with sizes ranging from 200 nm to 1 μm. Table V summarizes the results of EDS spot analysis.

A high magnification elemental mapping of the DT 500HV and QT500HV after soaking at 650 °C for 40 hours is shown in Figure 10. The results confirm the massive precipitation of alloy carbides on the prior cellular boundaries (*i.e.*, Intercellular micro-segregation) in DT sample. As it is shown in Figure 10(a) and corresponding elemental mapping, intercellular micro-segregation enriched in C and alloying elements served as preferential sites for the precipitation and growth of the alloy carbides at the vicinity of coarse V(C,N) particles, in agreement with previous SEM, and thermodynamic simulations results. A further effect is the enrichment (micro-segregation) of Si to the cell boundaries. Indeed, the average concentration of Si at the cell boundaries was around 1.3 ± 0.2 wt pct, while the matrix showed 0.70 ± 0.1 wt pct Si, as compared to the nominal wt pct of 0.95 in a qualitative agreement with DICTRA simulations in Figure 8(b). The elemental distribution in QT is more homogeneous [Figure10(b) and corresponding color mappings], confirming that some homogenizing, even if partially, could occur

during austenitization, and that the number of coarse V(C,N) is increased in the QT.

The coupled EBSD measurements on the same areas in Figure 10 are depicted in Figure 11. In band contrast (BC) maps, boundaries with misorientation angles larger than 10° are shown in black, and those larger than 2 deg are in white [Figures11(a) and (b) for DT500HV, and QT500HV soaked for 40 hours at 650 °C, respectively]. It is noteworthy mentioning that, the parallel crystal alignment representing the blocks of the lath martensite is still quite stable. Moreover, V(C,N), Cr_7C_3, and $Cr_{23}C_6$ phase maps are overlaid on BC maps. With the phases present in the microstructure, it is now possible to postulate that most of the Cr-rich carbides precipitated on the martensite substructure boundaries should have been of Cr_7C_3 type. V(C,N) is also detected in line with EDS mapping and spot analysis. Small amount of the equilibrium phase $Cr_{23}C_6$ is found as well. Unfortunately, a reliable structure was not available for M_2C and equilibrium M_6C in the database (*i.e.*, Mo-rich carbides); however, their presence was confirmed with certainty using the BSE micrographs/EDS analysis in Figure 9.

The corresponding misorientation angle distributions are shown in Figure 11(c). To quantify the martensite substructure size (*i.e.*, block and lath), several measurements at higher magnification were performed. According to Morito *et al.*,[39] in a medium carbon martensitic steel, martensite packets consist of fine blocks whose
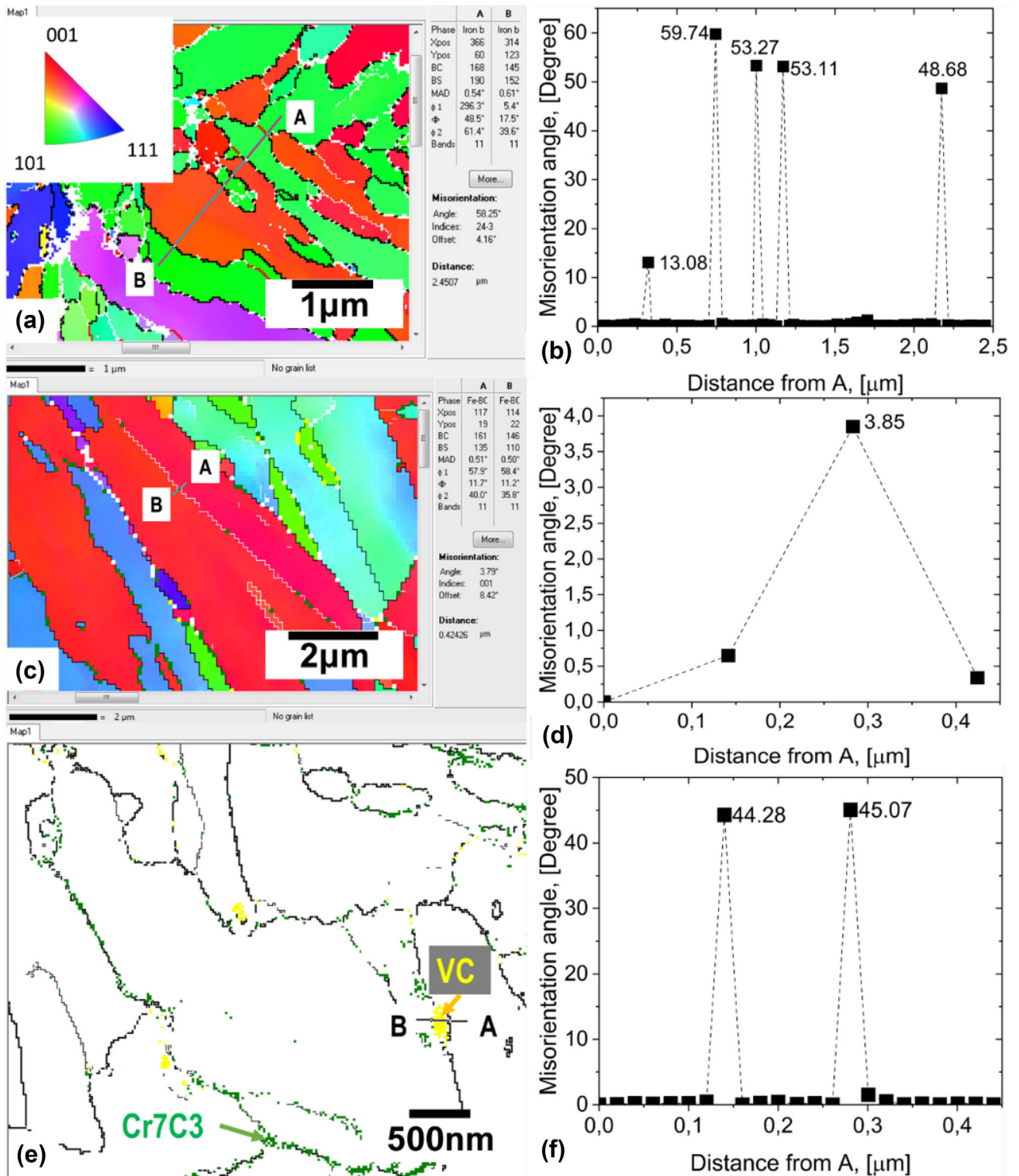
Fig. 12—(*a*) IPF-X map, showing blocks of laths with single orientation, (*b*) corresponding point to point (A to B) misorientation highlighting neighboring blocks misorientation angles, (*c*) IPF-X map showing laths of alternating contrast within a block, (*d*) corresponding point to point (A to B) misorientation showing a misorientation angle of 3.8 deg between the neighboring points of the laths with alternating contrast (>2 deg is in white, and > 10 deg is in black), (*e*) carbides phase map for the ease of demonstration, and (*f*) corresponding point by point misorientation (A to B, passing from the matrix to carbide), showing peaks at ~ 44–45 deg.

Table VI. Block Size Statistics in DT and QT Samples Soaked for 40 h at 650 °C

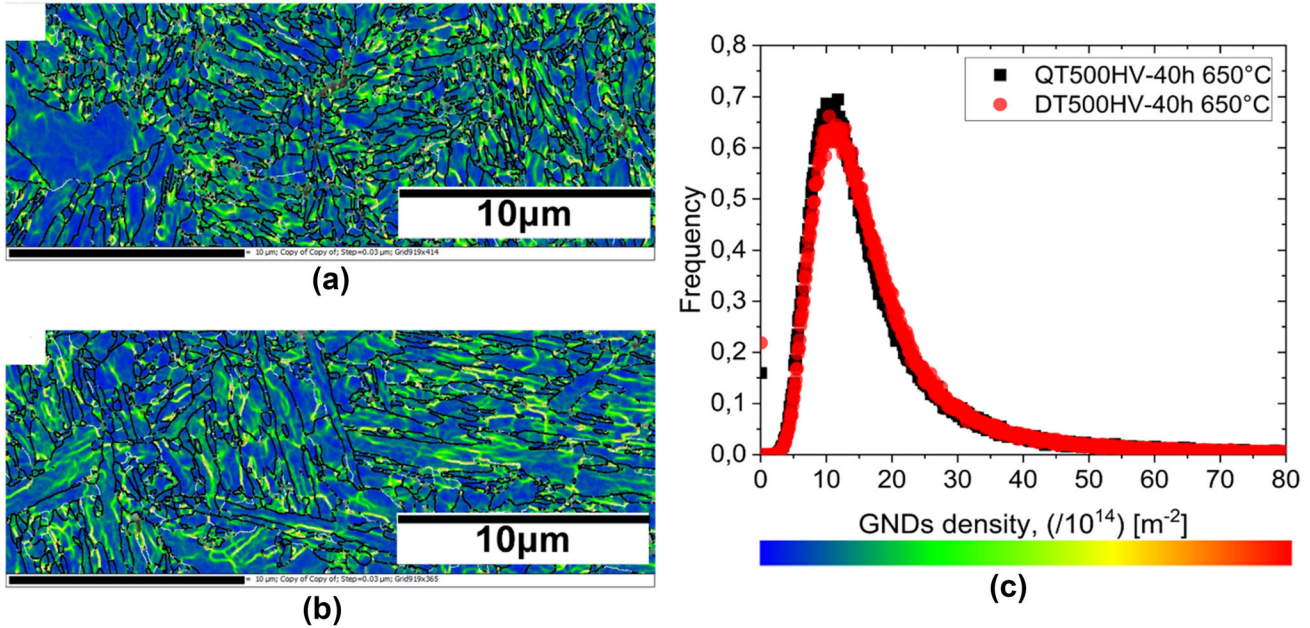|	EBSD -Magnification	Step Size (μm)	Mean (μm)	Standard Deviation	Variance	Size of Dataset
QT	10kX	0.03	0.50	0.58	0.33	4911
DT	10kX	0.03	0.35	0.41	0.17	7533

Fig. 13—GNDs density maps after 40 h soaking at 650 °C, overlaid by boundaries with misorientation angles of > 2 deg, and > 10 deg: (*a*) DT500HV, (*b*) QT500HV, and (*c*) GNDs density distribution.

Table VII. Hall Petch and Dislocation Density Strengthening Contribution in QT500HV and DT500HV Soaked for 40 h at 650 °C

	Hall–Petch (MPa)	Dislocation Strengthening (MPa)	Total Martensite Strengthening Eq. [6] (MPa)	ΔHV Model-Eq. [5] (HV1)
QT	296	302	598	~ 19
DT	354	293	647	

width is less than 1 μm. Blocks consist of laths with a single variant, and six blocks with different orientations exist in a packet. Given a list of possible 24 martensite variants from parent austenite and the rotation in degrees from variant 1 it was shown the rotation in degrees for block boundaries is all > 10 deg.[39] On the other hand, most of the lath boundaries have misorientation angles < 3 deg. It has also been observed that boundaries with larger misorientation angles (>2 deg) often correspond to lath boundaries separating laths or groups of laths with alternating contrast.[39] In Figures 12(a) and (b), the inverse pole figure map (IPF-X) and corresponding rotation misorientations in neighboring blocks (points A to B) are shown, respectively. The misorientation angles agree quite well with

those of K–S orientation relationships. The corresponding peaks in Figures 11(c) also confirm this observation. As the main intention is to measure the block width in DT and QT, this confirmation on the critical misorientation angle (*i.e.*, > 10 deg) selection had to be shown. Next is lath structure confirmation. In agreement with the work of Morito *et al.*,[39] in the current samples, the misorientation within blocks (*i.e.*, lath boundaries) was normally below 2 deg, while larger than 3 deg misorientation angles were corresponding to the separation of laths with different contrasts as shown in Figures12(c) (IPF-X map) and corresponding misorientation seen in Figure12(d). Finally, as it can be observed in Figures 12(e) and (f), the misorientation angle of a phase boundary (*e.g.*, V(C,N) and matrix) peaks at ~
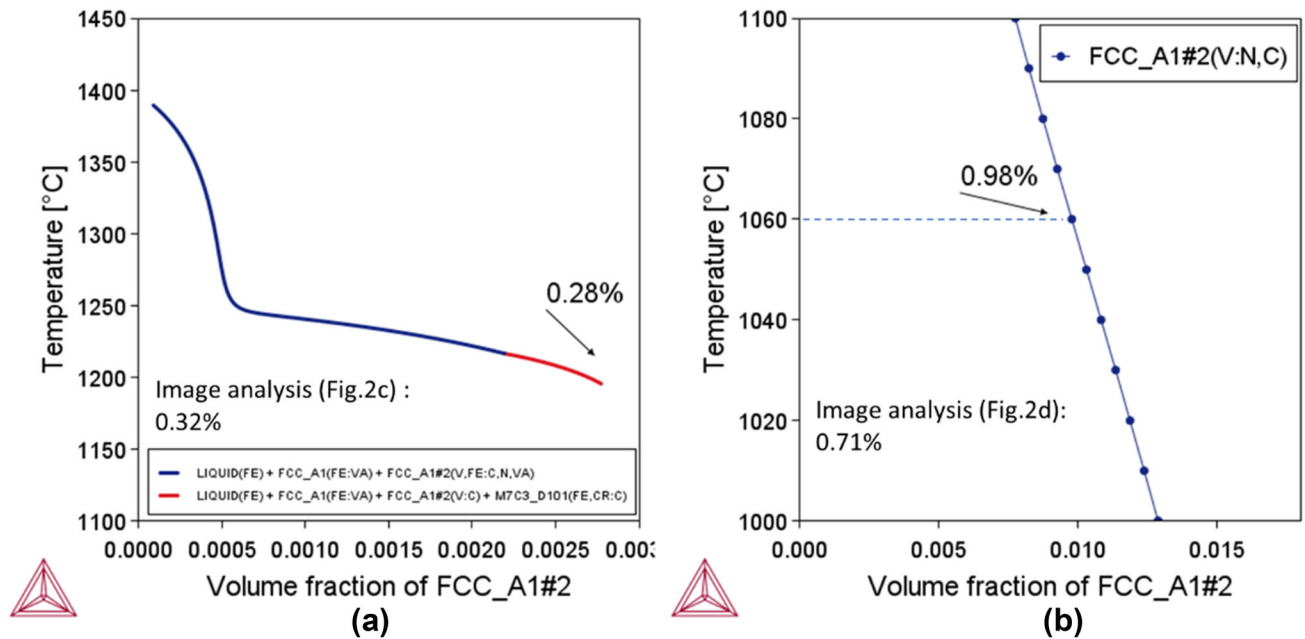
Fig. 14—Thermo-calc simulations of, (*a*) volume fraction of the coarse V(C,N) after rapid solidification in AB specimen (Scheil simulations), and (*b*) volume fraction of coarse V(C,N) under equilibrium condition at the austenitization temperature of 1060 °C in Q specimen.

44–45 deg. Around this misorientation angle, a peak in Figures 11(c) is observed for both samples and was removed for the calculation of block size.

With this information, now it is more convenient to elaborate on Figure10(c). First, it is possible to postulate that the lath size seems to be finer in QT sample given its larger frequency in Figure10(c); however, it is well known that lath width (*e.g.*, low angle boundaries.) is not a decisive factor in grain boundary (Hall–Petch) strengthening of Fe-C martensite. Instead block width (*e.g.*, high angle boundaries) is the smallest subunit in martensite hierarchy that shows a valid correlation to hardness (Strength) using Hall–Petch relation.[40,41] Indeed, Morito *et al.*[40] and other researchers showed that the block size can be considered as the "effective" grain size in Fe-C martensite for Hall–Petch strengthening considerations.[42–44] In this regard, the block width in DT (350 nm) was slightly finer than that of QT (500 nm) when considering a threshold of > 10 deg misorientation to calculate the block size using line intercept method (Table VI). Of course, the prior austenite and packet boundaries are also of high angle and could affect the block width measurement results. However, given the high magnification (10kX) of scans, it can be accepted that just a few packet and prior austenite boundaries are included in the measurements which will not affect the statistical validity of the block width values.

Figure 13 depicts the GNDs densities for DT500HV and QT500HV samples soaked for 40 hours at 650 °C, calculated using EBSD scans and Kernel Average Misorientation (KAM) maps overlaid by misorientation angles over 10 deg in black and over 2 deg in white. For the GNDs density calculation, the threshold value of 5 deg was applied. According to Calcognotto *et al.*,[45]

as a result of the lattice distortion during martensite transformation, misorientations greater than 2 deg can exist in a single martensite variant as seen, and confirmed experimentally in Figure 12(d). Therefore, it is more reasonable to use 5 deg as the threshold. From Figures 13(a) and (b), it is obvious the dislocation density is larger within the blocks and plausibly at the low angle lath boundaries. It was argued by Galindo-Nava *et al.*[41,46] that laths, within blocks, form to minimize the strain energy resultants of the lattice distortions around carbon atoms during martensite transformation, and the lattice strain is accommodated by the interfacial dislocation generation at the lath boundaries, accordingly carbon atoms redistribute to segregate at the lath boundary and intra-lath dislocations, as experimentally showed by atom probe tomography.[44] In both samples, there are areas within the blocks with the absence of low angle misorientation boundaries manifesting low dislocation density, representative of the significant dislocation recovery and possibly partial recrystallization of the lath substructure within those blocks by long-time holding at 650 °C in agreement with SEM results. By looking at Figure 13(c), there is not any significant difference between DT and QT in terms of GNDs density, where the distribution plots of GNDs nearly lay on each other showing a peak at $1.05 \times 10^{15}/m^2$, and $1.11 \times 10^{15}/m^2$, for DT and QT, respectively. This was also shown in the work of Yuan *et al.*,[18] where regardless of initial dislocation density, in both DT and QT samples, dislocation density dropped heavily and stabilized to similar levels during the first hours of soaking at elevated temperatures. Same behavior has been also evident and well established in the realm of wrought hot work tool steels.[47]

IV. DISCUSSION

The experimental results (Figure 4) clearly showed that the tempering resistance in DT specimens was significantly higher than those of QT. This behavior was independent of the RA decomposition during tempering (specific to DT), as prior to the tests, samples were all double tempered at temperatures over the secondary hardening peak with the aim to transform all RA to carbides and martensite (ferrite), afterward tempering resistance tests were performed on samples with a similar tempered hardness. Moreover, as depicted by GNDs density distribution, the final dislocation density of lath martensite was similar after 40 hours holding at 650 °C regardless of direct tempering from the as-built condition or quenching and tempering. However, after completion of tempering resistance tests, DT samples were still ~ 30 to 55 HV1 harder than QT counterparts. From the experimental hardness measurements, after 40 h soaking at 650 °C, QT420HV and DT420HV showed hardness of 316 ± 1 HV1 and 347 ± 4 HV1, respectively, and QT500HV and DT500HV showed hardness of 301 ± 3 HV1 and 355 ± 3 HV1, respectively (see Figure 4, and Electronic Supplementary Table S1). Given the identical activation energies at both temperatures, close to that of diffusion of substitutional alloying elements in ferrite, the same softening mechanism is expected for all samples which must be discussed in view of the microstructural features presented in the previous section.

For this purpose, a reference to the work of Galindo-Nava[41] on the modeling of the strength and hardness of tempered martensite is used. In this model, strengthening is attributed to (i) Hall–Petch, considering the width of the blocks as the smallest constituent of lath martensite characterized by high angle boundaries,[40] (ii) dislocation, and (iii) particle (tempering carbides) strengthening, and the last contributor is solid solution strengthening which plays a minor role in tempered martensite strength.[41] In this model, yield strength (σ_Y) is roughly equal to 110 MPa + 2.507 times Vickers hardness[46,48] Eq. [5]. Accordingly, in this equation, apart from lattice friction stress (σ_0) roughly equal to 50 MPa,[41] three strengthening contributions are considered in defining the strength of tempered martensite, namely martensite strengthening ($\sigma_{\mathrm{Martensite}}$), *i.e.*, combination of Hall–Petch and dislocation strengthening, precipitation hardening (σ_P), and substitutional solid solution strengthening (σ_{ss}).

$$\sigma_Y = 110 + 2.507(HV)$$
$$= \sigma_0 + \left(\sigma_{\mathrm{Martensite}}{}^2 + \sigma_p{}^2\right)^{0.5} + \sigma_{ss}. \qquad [5]$$

The effective martensite strength ($\sigma_{\mathrm{Martensite}}$), without the contribution of precipitates (σ_P), is given by the combination of Hall–Petch and dislocation strengthening, and is modeled using Eq.[6],

$$\sigma_{\mathrm{Martensite}} = K_d / \sqrt{d_{\mathrm{block}}} + m\alpha Gb\sqrt{\rho}. \qquad [6]$$

In Eq. [6], the Hall–Petch constant (K_d) can vary from 100 to 300 MPa $\mu\mathrm{m}^{1/2}$ depending on which boundaries are considered (*e.g.*, block, packet, or prior austenite boundaries). As mentioned, backed by strong evidence, it is well accepted that block boundaries are the most effective contributors to the grain boundary strengthening of martensite, and a value of 210 MPa $\mu\mathrm{m}^{1/2}$ is proposed as the Hall–Petch constant when block width (d_{block}) is taken into account.[40,49] In dislocation strengthening model, m is the average Taylor factor, α is a constant, G is the shear modulus, b is the Burger's vector, and ρ is the dislocation density. In this regard, following the work of Krauss *et al.*,[50] m was set to 2.75 often used for BCC structures, α was set to 0.166, G was assumed to be 80 GPa, and the Burgers vector was set to 0.248 nm for a $\langle 111 \rangle$ slip direction. It must be mentioned that interstitial solution strengthening related to the C atoms is included in the dislocation strengthening term as substantial amount of C atoms segregate to dislocation strain fields (martensite lath boundaries) in low and medium carbon steels.[41,51,52]

σ_p, becoming effective after tempering, is defined by Eq. [7], where r_p is the particle (secondary carbide) radius and f_p is the fraction of particles.[41]

$$\sigma_P = 0.26 \frac{\mu b}{r_p} f_p^{0.5} \ln\left(\frac{r_p}{b}\right) \qquad [7]$$

Finally, Eq. [8] can be used for the substitutional solid solution strengthening, where x_i is the atom fraction of substitutional element i, β_i is the constant correlated to lattice misfit and modulus difference of element i compared with that of iron.[41,46]

$$\sigma_{ss} = \sum_i \left(\beta_i^2 x_i\right)^{0.5} \qquad [8]$$

The intention of using the models in Eqs. [5] through [8] is to find the possible mechanisms to explain the enhanced temper resistance for the DT samples, and therefore, the calculations should be considered as *comparative* in nature. In this regard, the substitutional solid solution strengthening in Eq. [8] can be neglected in our current calculations as materials are identical in chemistry, and long-time holding at 650 °C most probably results in the depletion of the matrix from substitutional alloying elements due to the formation of carbides. Indeed, in quenched state where the matrix is supersaturated, the substitutional solid solution strengthening in H13 is only 90–115 MPa,[53] so this value drops heavily after long-time tempering, accordingly any difference in DT and QT becomes insignificant. Therefore, in current calculations, a similar strengthening contribution of substitutional solution in over-tempered samples for both alloys was assumed.

Table VIII. Calculated matrix Chemical Composition of AB and Q Martensite Considering the Depletion of V, C, and N During Rapid Solidification and Austenitization Process, Equilibrium Volume Percent of V(C,N) at 650 °C (Tempering Carbide) is Shown for Both Conditions

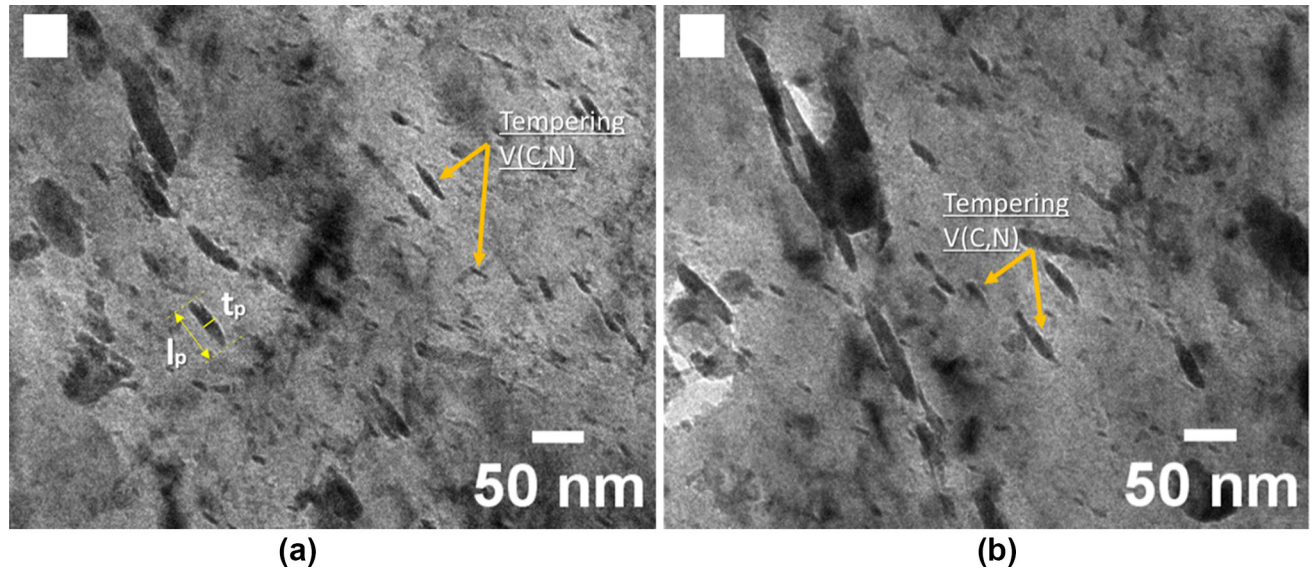| Matrix Composition (Martensite)	C	Cr	Mo	V	Si	Mn	N (PPM)	Equilibrium Tempering V (C, N) vol. Fraction at 650 °C
AB	0.39	5.11	1.59	0.80	0.95	0.30	130	0.0102
Q	0.35	5.11	1.57	0.58	0.95	0.30	30	0.0064

Fig. 15—TEM images of (*a*) DT, and (*b*) QT specimens.

Table IX. Length, Thickness, and Equivalent Particle Radius of Secondary (Tempering) V(C,N)

	l_p (nm)	t_p (nm)	Equivalent r_p (nm)	Size of Data Set
DT	33 ± 17	11 ± 4	7 ± 3	19
QT	44 ± 31	13 ± 4	9 ± 5	25

Table X. Nanosized Secondary V(C,N) Contribution to Strengthening in QT500HV and DT500HV Soaked for 40 h at 650 °C

	f_p	Equivalent r_p (nm)	Strengthening Eq. [7] (MPa)	ΔHV Model-Eq. [5] (HV1)
DT	0.0102	7 ± 3	242	~ 33
QT	0.0064	9 ± 5	160	

A. *Effect of Martensite Substructure and Dislocation Density on the Tempering Resistance*

Focusing on the $\sigma_{martensite}$ for the current specimens, both d_{block} and GNDs density were quantified. Although EBSD does not give insights to the statistically necessary dislocations, it is plausible that the geometrically necessary dislocations are the main source of the lath martensite strength, as the dislocation fields at the lath boundaries are generated to accommodate the lattice strain. GNDs density distribution in Figure 13 peaked at 1.05×10^{15} m^{-2} and 1.11×10^{15} m^{-2} for DT and QT, respectively. These numbers are in the range of the dislocation density measured, using X-ray diffraction (XRD) and transmission electron microscope (TEM) analysis, in a wrought H13 tempered at 650 °C,[54] and roughly an order of magnitude lower than that of as-quenched H13, and quenched Fe−0.4C, measured using TEM, and therefore seem to be reliably measured.[55]

The difference in strengthening of martensite in over-tempered DT and QT samples calculated using Eq. [6] is shown in Table VII. The dislocation density

does not play any role in strengthening difference, while finer block size in DT contributes to a higher strength, by ~ 50 MPa, yielding a total strengthening of ~ 19 HV1 in hardness. This difference is lower than the experiments, and the missing part (~ 11–36 HV1) cannot be described simply by the block size refinement (Hall–Petch) achieved by fast solidification, characteristics of L-DED. Indeed, even the finer block width is probably due to higher carbon supersaturation in as-built martensite compared with that of Q specimen, where in the latter, some carbon was depleted from matrix to form vanadium-rich carbides during the austenitization. According to the pioneering work of Morito et al.,[40,49] martensite block width is inversely proportional to the C content in Fe–C martensite.

B. Effect of Secondary (Tempering) M(C,N) Carbides on the Tempering Resistance

1. Volume fraction

By using image analysis and EDS mapping combined with EBSD analysis (Figures 2, 10, and 11, respectively), it was shown that in AB samples the vol pct of coarse V(C,N) carbides was lower than that of Q one (i.e., 0.32 vol pct vs. 0.71 vol pct). This was attributed to the elimination of the austenitization step which otherwise leads to the precipitation of excess stable V(C, N) in quenched specimen. According to Scheil simulations in Figure 14(a), the volume fraction of V(C,N) precipitated during the non-equilibrium solidification is ~ 0.28 pct, very close to that of image analysis results of AB specimen [0.32 pct, see Figure 2(c)]. Accordingly, volume fraction of V(C,N) at the austenitization temperature of 1060 °C under equilibrium conditions is 0.98 pct [Figure 14(b)], close to that measured by image analysis [0.71 pct, see Figure 2(d)]. This means that in quenched martensite available V, C, and N in supersaturated solid solution to form fine tempering V(C,N) during the tempering process were less than that of the AB specimen. To demonstrate this, Table VIII summarizes equilibrium Thermo-Calc calculations of the vol pct of tempering V(C,N) at 650 °C in AB and Q martensite. These calculations were made by considering the depletion of V, C, and N, forming coarse V (C, N), from the matrix during the solidification (i.e., stringers of V(C,N) in the as-built martensite with a vol pct of 0.32), and austenitization process (i.e., sum of vol pct of stringers, and globular V(C,N) in quenched martensite equal to 0.71). It is evident that due to the less available elements V, C, and N in quenched martensite, the equilibrium vol pct of secondary (tempering) V(C, N) is only ~ 0.64 pct, much lower than that of AB specimen (i.e., ~ 1.02 pct).

Under the assumption that the system moves toward equilibrium after long-time holding of 40 hours at 650 °C, the calculated vol pct of secondary V(C,N) at 650 °C (Table VIII) was used as an input for precipitation strengthening modeling.

2. Precipitate size

Secondary (tempering) V(C,N) size was measured using TEM analysis [Figures 15(a) and (b)]. Given the morphology of the particles, an equivalent circular particle radius of r_p (i.e., $r_p = \sqrt{\frac{t_p l_p}{2\pi}}$) was measured, where t_p and l_p are particle thickness and length, respectively [see Figure 14(a)]. The mean values are reported in Table IX.

3. Precipitation strengthening contribution

By knowing the radius, and estimation of the vol pct of the secondary (tempering) V(C,N), it is now possible to derive their strengthening contribution using Eq [7].[41,46] The strengthening effect of secondary (tempering) V(C, N) in DT and QT was estimated to be ~ 242 MPa and 160 MPa, respectively, which is equivalent to ~ 33 HV1 hardness difference (Table X).

Along with its higher vol pct, the secondary (tempering) V(C,N) in DT was slightly finer than that of QT, meaning DT comprised a larger number density of secondary (tempering) V(C,N). While the larger vol pct of V(C,N) in DT is a direct consequence of skipping austenitization step, its slightly finer size can be related to the complementary effect of larger dislocation density and finer substructure size in rapidly solidified AB specimen prior to tempering, providing increased nucleation sites for the secondary (tempering) carbide precipitation.

With regard to the other types of alloy carbides, it was shown that all Cr- and Mo-rich carbides had grown to sizes of ~ 50–200 nm [see Figure 8]. Only the most thermally stable secondary (tempering) V(C,N) was in the range of ~ 20 nm in equivalent diameter, which can effectively contribute to a difference in particle strengthening contributions of the two alloys according to Orowan mechanism Eq. [7]. This is discussed in detail in the work of Sonderegger et al.[11] as well as Eser et al.[37] who showed that in H11 and H13 steels the secondary (tempering) V(C,N) carbide strengthening at holding temperatures of 650 °C and above is four times (i.e., ~ 80 MPa) more effective than those of Cr_7C_3, $Cr_{23}C_6$, and Mo_6C (i.e., ~ 20 MPa) simply due to the much slower coarsening kinetics of the former. Indeed, in the work of Sonderegger et al.[11] using TEM, the secondary (tempering) V(C,N) average radius was calculated to 11 (max. 51 nm) and 27 nm (max. 51 nm) after 24 hours holding at 650 °C, and 680 °C respectively, while Cr-rich carbides and Mo-rich M_6C were coarsened to an average size of 55 and ~ 70 nm, respectively. TEM observations in this work, at least for the coarsened M(C,N), are in a good agreement with the work of Sonderegger et al.[11]

C. Total Strengthening Contribution in Over-Tempered Condition

According to Norström model,[52] by using the linear sum of the strengthening contributors, the hardness difference between DT and QT (i.e., 33 + 19 = 52 HV1) perfectly matches with those of measured values (i.e., 31–54 HV1). However, given the nature of multiple strengthening mechanisms, (i.e., martensite and precipitation hardening) and the suggestion in Eq. [5],[41,46] a rule of mixture was proposed to calculate the total

strengthening. This suggestion seems to be reasonable as the carbide precipitation during tempering reduces the dislocation strengthening component of lath martensite through reduction of carbon atoms segregated to the lath boundaries. Moreover, as tempering carbides mainly precipitate on martensite substructure boundaries (*e.g.*, lath and block boundaries), the contribution of Hall–Petch component of lath martensite strengthening and that of precipitation hardening should be formulated through a rule of mixtures and cannot be precise through a linear sum of the strengthening contributors as both act as barriers to dislocation motion.

The overall results are listed in Table XI. The hardness difference for the two specimens in view of the martensite strength, and increased vol pct of secondary (tempering) V(C,N) is around 29 HV1. This difference is lower than that witnessed in experiments. However, this is close enough to accept that the superior tempering behavior of DT is a consequence of rapid solidification (*i.e.*, finer martensite substructure as a result of larger C supersaturation, and higher cooling rates), and skipping the austenitization step (*i.e.*, larger V, C, and N in solid solution by avoiding excessive coarse V(C,N) precipitation). More importantly, it is

evident that the major cause of the strengthening difference in DT and QT stems from the larger vol pct of very fine and stable V(C,N) rather than the substructure size (*i.e.*, 29 HV1 *vs*. 19 HV1).

D. *Additional Considerations*

It is repeatedly reported that silicon inhibits cementite precipitation in tool steels.[56–58] However, Si effect on cementite precipitation is debated by Kozeschnik and Bhadeshia.[59] These authors argue that Si partitioning is not a prerequisite for cementite precipitation in the highly supersaturated martensite, because the driving force for this reaction is large enough even for the para-equilibrium precipitation. Nevertheless, same authors claimed that experimental results suggest otherwise, and Miyamoto *et al*.[60] showed that para-cementite is difficult to form in the Si-added martensite due to the instability of cementite containing Si. The secondary (tempering) carbides in hot work tool steels with low Si concentration nucleate on the pre-existing cementite particles formed at the 4th stage of tempering, providing C to react with substitutional alloying elements (*e.g.*, Cr) or within the martensitic matrix. If in the presence of Si, cementite precipitation and growth are delayed, then

Table XI. Total Strengthening Difference in QT500HV and DT500HV Soaked for 40 h at 650 °C

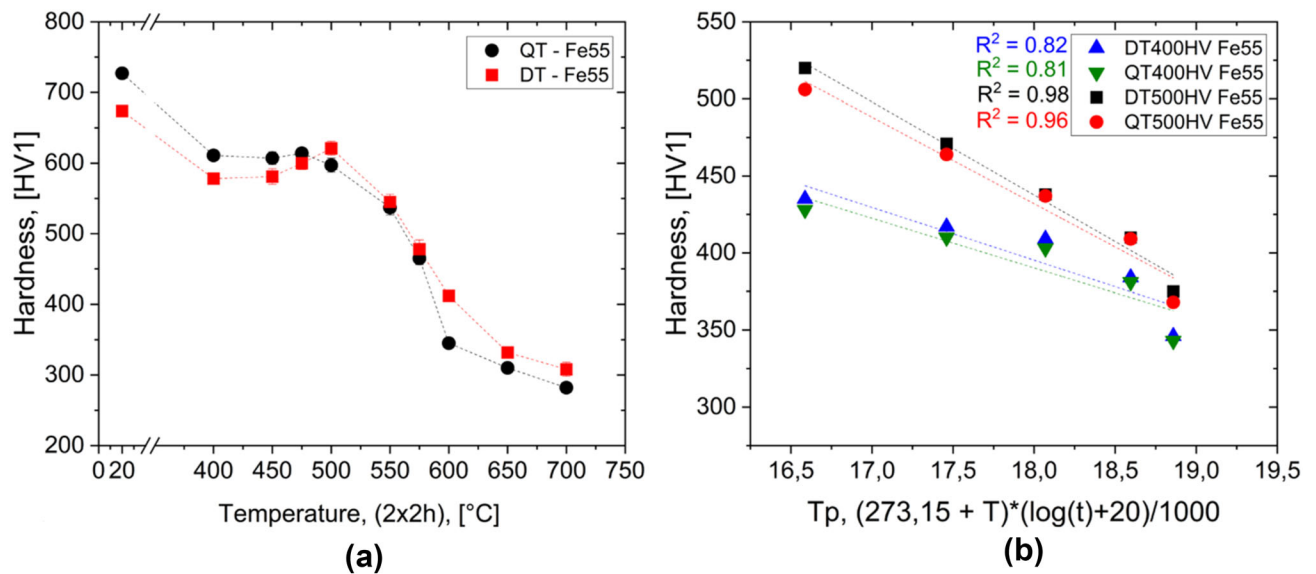|	$\sigma_{\text{Martensite}}$ (MPa)	σ_p Sec. V(C,N) (MPa)	$(\sigma_{\text{Martensite}} + \sigma_P)$ Linear sum (MPa)	ΔHV linear (HV1)	$(\sigma_{\text{Martensite}}^2 + \sigma_p^2)^{0.5}$ Eq. [5] (MPa)	$\Delta\sigma_Y$ Eq. [5] (MPa)	ΔHV Eq. [5] (HV1)
DT	647	242	889	~ 53	691	72	~ 29
QT	598	160	758		619		

Fig. 16—(*a*) Tempering curves of AB and Q Ferro 55 for 2 × 2 h tempering, and (*b*) Hardness *vs*. Tempering parameter (T_p), for up to 40 h over-tempering.

larger C is available for precipitation of secondary (tempering) carbides. As a result, the alloy carbide precipitation is anticipated. The anticipated alloy carbides formation in the presence of Si shifts the secondary hardening peak to lower temperatures, and reduces the tempering resistance simply because of anticipated coarsening. In the absence of Si, the alloy carbides precipitate at higher temperatures, because cementite forms easier, and its dissolution is a perquisite for the precipitation of alloy carbides. This is especially true for Cr-rich Cr_7C_3 carbides.[57] Micro-segregation of Si, as shown by EDS mapping as well as DICTRA simulations, and consequently less available Si in the core of the cell, might be the reason for the delayed carbide coarsening, especially Cr-rich carbides in the cell center of DT. This was clearly shown in the SEM images of Figures 7(c) and (d). Of course, higher concentration of carbon, and carbide forming elements at the cell boundaries still serves as the principal reason for the accelerated carbide precipitation and coarsening at those areas compared with the core.

E. Confirmation on the Effect of V on Tempering Resistance

In order to get a solid confirmation on the effect of V, as the main contributor to improved temper resistance in DT samples, authors L-DED processed a commercially available vanadium-free hot work tool steel powder known as Ferro 55 or X38CrMo7–2[61,62] with a nominal composition of 0.4C, 7.0 Cr, 2.5 Mo, 0.2 Si, 0.7 Mn, and Fe bal. Afterward, similar direct tempering, and quench and tempering experiments, followed by softening resistance tests were made on this AM tool steel. In this steel, carbon content is similar to H13, while Cr and Mo wt pct are even larger than that of H13, V is absent, but unfortunately, Si has also quite low wt pct, making the conclusion on Si effect difficult as two factors changed at the same time. The material was austenitized at 1000 °C for 15 min to avoid grain coarsening.

The tempering curves in Figure 16(a) show quite similar behavior to H13, as the secondary hardening peak is shifted to higher temperature for the DT, and a higher hardness is recorded for DT after the secondary hardening peak, because of RA decomposition (~10 vol pct[63]). However, the hardness difference between the two tempering scenarios is much smaller compared with H13 (see Figure 2 for comparison).

First interesting observation is related to 2 × 2 hours tempering [Figure 16(a)], where the sudden drop in hardness at high tempering temperatures is evident (i.e., 550 °C and above). At these tempering temperatures, where Cr and Mo carbide coarsening is enhanced,[11,37] the absence of thermally stable secondary (tempering) V(C,N) leads to a significant softening compared with H13. For instance, H13 hardness after 2× 2 hours tempering at 650 °C was 360 HV1, and 415 HV1 for QT, and DT, respectively [see Figure 2(a)], while in Ferro 55 steel, these values dropped by at least 60 HV1

to 300 HV1, and 320 HV1, for QT, and DT, respectively.

The main goal of this experiment was to evaluate the temper back or softening resistance behavior in this V-free alloy [Figure 16(b)]. It is clearly demonstrated, as opposed to H13, there are no differences between DT Ferro55 and QT Ferro 55 hardness over the whole holding period of 40 hours, at the test temperature of 600 °C. At this testing condition (i.e., 40 hours at 600 °C), the difference between QT and DT H13 was ~ 30 HV1, both showing significantly higher hardness than Ferro 55 counterparts (see Figure 4 and electronic supplementary Table S3). The Avrami exponents of ~ 0.4 and the softening activation energies ~ 220 kJ/mol for Ferro 55 were measured, and the details can be found in electronic supplementary Figures S1, S2, and Table S4.

This observation strongly confirms the significant effect of larger vol pct of secondary V(C,N) in improving the temper resistance of DT H13 compared with QT H13 (i.e., by avoiding coarse V(C,N) precipitation during the austenitization process). Moreover, as it can be appreciated from Figure 16(b), at elevated temperatures and long holding periods, Cr and Mo secondary carbides with lower resistance to coarsening compared with that of V(C,N) do not cause any strength difference in over-tempered condition between the DT and QT Ferro 55 specimens. Therefore, current results also confirm the validity of the earlier assumption made by authors regarding excluding any possible role of Cr and Mo carbides in particle strengthening difference of over-tempered DT and QT H13 (Section IV–B).

F. Suggestions on Alloy Design for Laser-Based AM Processes

From a technological viewpoint, the current results open new ways in the realm of design for leaner AM tool steels. Authors believe that in rapidly solidified vanadium containing hot work tool steel, elimination of costly austenitization step imposes a twofold thermal stability and strengthening effect in tempered martensite:

(i)   RA decomposition during tempering increases the thermal stability by shifting the secondary hardening peak to higher temperatures.

(ii) By eliminating austenitization step, thus preserving both C and V in super saturated solid solution for later secondary (tempering) V(C,N) precipitation, a strong increase in tempering resistance can be achieved.

Therefore, by exploiting direct tempering from AB condition, AM hot work tool steels, showing promising thermal stability, with even lower nominal carbon contents compared to wrought counterparts, can be introduced. Reduction of C plays a significant metallurgical role in tackling the very common challenge of cold cracking in laser additive manufacturing of hot work tool steels.[64–66]

V. CONCLUSIONS

In this work, the tempering resistance of AISI H13 hot work tool steel fabricated by L-DED was investigated, and the main conclusions are summarized as follows:

- A shift in secondary hardening peak toward higher temperatures (~20 °C) was witnessed in samples directly tempered (DT) from the as-built condition compared with the quenched and tempered (QT) counterparts. Retained austenite (RA) decomposition in DT was marked as the most significant mechanism in this regard.
- Tempered hardness of DT specimens was systematically higher than that of QT above the secondary hardening peak temperature over a large tempering temperature range, confirming the higher tempering resistance of DT. This could be verified even over a long over-tempering time of 40 hours at elevated temperatures of 600 °C and 650 °C, showing a hardness difference of ~ 30–50 HV between DT and the QT.
- The activation energies of transformations causing softening were similar for both tempering scenarios, equal to that of diffusion of substitutional alloying elements in ferrite. Therefore, the higher tempering resistance of DT was discussed in view of the different strengthening effects calculated according to microstructural analyses.
- The main contributor to the enhanced temper resistance of DT was the increased vol pct of *fine* and the most thermally stable *secondary (tempering)* V(C,N) because of elimination of austenitizing process. *Coarse stable annealing* V-rich carbonitrides precipitation during the austenitization reduces the available V and C in the supersaturated quenched martensite for a later precipitation of *fine* and thermally stable *secondary* (tempering) V(C,N) during the tempering process.
- Martensite substructure (block) refinement, resultant of rapid solidification and larger C supersaturation, introduced a complementary strengthening effect on the tempering resistance of DT specimens through Hall–Petch strengthening mechanism and by providing increased nucleation sites for tempering carbides precipitation. After 40 hours tempering at 650 °C, dislocation density within the blocks and at the lath boundaries was similar for both QT and DT, excluding any dislocation strengthening effect on the enhanced temper resistance of the directly tempered samples after long holding times.
- The effect of V (*i.e.*, *tempering* V(C,N)) was validated by assessing an L-DED processed **vanadium free** hot work tool steel (Ferro 55). While a secondary hardening peak shift due to RA decomposition was evident (~15 °C), the DT and QT samples showed no clear hardness difference during long-time temper resistance tests as opposed to **vanadium containing** H13.

SUPPLEMENTARY INFORMATION

ACKNOWLEDGMENTS

COMPETING INTEREST

The authors declare that they have no known competing financial interests or personal relationships that could have appeared to influence the work reported in this paper.

OPEN ACCESS

REFERENCES

1. G.A. Roberts, R. Kennedy, and G. Krauss: *Tool Steels, 5th Edition*, ASM International, 1998.
2. A.C.F. de Silveira, R. Fechte-Heinen, and J. Epp: *Addit. Manuf.. Manuf.*, 2023, vol. 63, p. 103408.
3. S. Choi, H. Kim, J. Sung, D. Lee, and J. Seo: *Materials*, 2020, vol. 13, p. 5068.
4. Z. Zhao, M. Perini, P. Bosetti, and M. Pellizzari: *Steel Res. Int.*, 2023, vol. 94, p. 2370041.
5. F. Deirmina, S. Amirabdollahian, L. Harris, E. Bettini, R. Siriki, M. Pellizzari, P. Bosetti, and A. Molinari: *Met. Mater. Int.*, 2023, vol. 29, pp. 2940–954.
6. M. Laleh, E. Sadeghi, R.I. Revilla, Q. Chao, N. Haghdadi, A.E. Hughes, W. Xu, I. De Graeve, M. Qian, I. Gibson, and M.Y. Tan: *Prog. Mater. Sci.*, 2023, vol. 133, 101051.
7. T. Feldhausen, M. Paramanathan, J. Heineman, A. Hassen, L. Heinrich, R. Kurfess, K. Fillingim, K. Saleeby, and B. Post: *J. Manuf. Mater. Process.*, 2023, vol. 7, p. 74.

8. J. Bennett, D. Garcia, M. Kendrick, T. Hartman, G. Hyatt, K. Ehmann, F. You, and J. Cao: *J. Manuf. Sci. Eng.*, 2018, vol. 141, 021019.
9. J. Mazumder, J. Choi, K. Nagarathnam, J. Koch, and D. Hetzner: *JOM*, 1997, vol. 49, pp. 55–60.
10. P. Bajaj, A. Hariharan, A. Kini, P. Kürnsteiner, D. Raabe, and E.A. Jägle: *Mater. Sci. Eng. A*, 2020, vol. 772, 138633.
11. B. Sonderegger, E. Kozeschnik, H. Leitner, H. Clemens, J. Svoboda, F.D. Fischer, and P. Starson: *Steel Res. Int.*, 2010, vol. 81, pp. 64–73.
12. T. Yuxin, L. Minghe, C. Haiyan, Y. Guanghong, and X. Zhou: *Baosteel Tech. Res.*, 2010, vol. 4, pp. 58–64.
13 G. Krauss: *Steel Res. Int.Int*, 2017, vol. 88, p. 1700038.
14. J. Zhu, Z. Zhang, and J. Xie: *Mater. Sci. Eng. A*, 2019, vol. 752, pp. 101–14.
15. F. Deirmina, N. Peghini, B. AlMangour, D. Grzesiak, and M. Pellizzari: *Mater. Sci. Eng. A*, 2019, vol. 753, pp. 109–21.
16. S. Amirabdollahian, F. Deirmina, M. Pellizzari, P. Bosetti, and A. Molinari: *Mater. Sci. Eng. A*, 2021, vol. 814, 141126.
17. J. Krell, A. Röttger, K. Geenen, and W. Theisen: *J. Mater. Process. Technol.*, 2018, vol. 255, pp. 679–88.
18. M. Yuan, Y. Cao, S. Karamchedu, S. Hosseini, Y. Yao, J. Berglund, L. Liu, and L. Nyborg: *Mater. Sci. Eng. A*, 2022, vol. 831, 142322.
19. M. Pellizzari, S. Furlani, F. Deirmina, R. Siriki, B. AlMangour, and D. Grzesiak: *Steel Res. Int.*, 2020, vol. 91, p. 1900449.
20. E.B. Fonseca, A.H.G. Gabriel, J.A. Ávila, R.F. Vaz, D.B. Valim, I.G. Cano, and É.S.N. Lopes: *Addit. Manuf.*, 2023, vol. 78, 103862.
21. M. Pellizzari, D. Massignani, S. Amirabdollahian, and F. Deirmina: *Steel Res. Int.*, 2023, vol. 94, p. 2200449.
22. S. Amirabdollahian: Doctoral Thesis, University of Trento, Trento, 2023.
23. F. Deirmina, S. Amirabdollahian, M. Pellizzari, and A. Molinari: *Metals*, 2024, vol. 14, p. 112.
24. C.-Y. Chou, N.H. Pettersson, A. Durga, F. Zhang, C. Oikonomou, A. Borgenstam, J. Odqvist, and G. Lindwall: *Acta Mater.*, 2021, vol. 215, 117044.
25. P.J. Konijnenberg, S. Zaefferer, and D. Raabe: *Acta Mater.*, 2015, vol. 99, pp. 402–14.
26. J.-O. Andersson, T. Helander, L. Höglund, P. Shi, and B. Sundman: *Calphad*, 2002, vol. 26, pp. 273–312.
27. S. Amirabdollahian, F. Deirmina, L. Harris, R. Siriki, M. Pellizzari, P. Bosetti, and A. Molinari: *Scripta Mater.*, 2021, vol. 201, 113973.
28 F. Deirmina, L. Quarzago, D. Butcher, E. Bettini, S. Mehraban, J. Hann, N.H. Pettersson, N. Lavery, A. Röttger, and M. Pellizzari: *Mater. Sci. Eng. A*, 2024, vol. 901, p. 146554.
29. E.B. Fonseca, J.D. Escobar, A.H.G. Gabriel, G.G. Ribamar, T. Boll, and É.S.N. Lopes: *Addit. Manuf.*, 2022, vol. 55, 102812.
30. Z. Zhang, D. Delagnes, and G. Bernhart: *Mater. Sci. Eng. A*, 2004, vol. 380, pp. 222–30.
31. C. Li, Y. Han, E. Li, S. He, and J. Ren: *J. Materi Eng Perform*, 2022, vol. 31, pp. 4983–997.
32. Q. Zhou, X. Wu, N. Shi, J. Li, and N. Min: *Mater. Sci. Eng. A*, 2011, vol. 528, pp. 5696–700.
33. Y. Wang, K. Song, and Y. Zhang: *Mater. Res. Express*, 2019, vol. 6, 096513.
34. A. Ning, Y. Liu, R. Gao, S. Yue, M. Wang, and H. Guo: *JOM*, 2021, vol. 73, pp. 2194–202.
35. D. Ablitzer, J.P. Haeussler, K.V. Sathyaraj, and A. Vignes: *Philos. Mag. A*, 1981, vol. 44, pp. 589–600.
36. P.J. Alberry and C.W. Haworth: *Metal Sci.*, 1974, vol. 8, pp. 407–12.
37. A. Eser, C. Broeckmann, and C. Simsir: *Comput. Mater. Sci.*, 2016, vol. 113, pp. 280–91.
38. H.-H. König, N.H. Pettersson, A. Durga, S. Van Petegem, D. Grolimund, A.C. Chuang, Q. Guo, L. Chen, C. Oikonomou, F. Zhang, and G. Lindwall: *Acta Mater.*, 2023, vol. 246, 118713.
39. S. Morito, H. Tanaka, R. Konishi, T. Furuhara, and T. Maki: *Acta Mater.*, 2003, vol. 51, pp. 1789–799.
40. S. Morito, H. Yoshida, T. Maki, and X. Huang: *Mater. Sci. Eng. A*, 2006, vol. 438–440, pp. 237–40.
41. E.I. Galindo-Nava and P.E.J. Rivera-Díaz-del-Castillo: *Acta Mater.*, 2015, vol. 98, pp. 81–93.
42. J. Daigne, M. Guttmann, and J.P. Naylor: *Mater. Sci. Eng.*, 1982, vol. 56, pp. 1–10.
43. U.F. Kocks and H. Mecking: *Prog. Mater. Sci.*, 2003, vol. 48, pp. 171–273.
44. B. Hutchinson, J. Hagström, O. Karlsson, D. Lindell, M. Tornberg, F. Lindberg, and M. Thuvander: *Acta Mater.*, 2011, vol. 59, pp. 5845–858.
45. M. Calcagnotto, D. Ponge, E. Demir, and D. Raabe: *Mater. Sci. Eng. A*, 2010, vol. 527, pp. 2738–746.
46. E. Galindo-Nava, W. Rainforth, and P. Rivera-Díaz-del-Castillo: *Acta Mater.*, 2016, vol. 117, pp. 270–85.
47. J. Sjöström and J. Bergström: *J. Mater. Process. Technol.*, 2004, vol. 153–154, pp. 1089–96.
48. E.J. Pavlina and C.J. Van Tyne: *J. Mater. Eng. Perform.*, 2008, vol. 17, pp. 888–93.
49. A. Shibata, T. Nagoshi, M. Sone, S. Morito, and Y. Higo: *Mater. Sci. Eng. A*, 2010, vol. 527, pp. 7538–544.
50. S.C. Kennett, G. Krauss, and K.O. Findley: *Scripta Mater.*, 2015, vol. 107, pp. 123–26.
51. G. Krauss: in *Phase Transformations in Steels*, E. Pereloma and D.V. Edmonds, eds., vol. 2, Woodhead Publishing, 2012, pp. 126–50.
52. L.-Å. Norström: *Metal Science*, 1976, vol. 10, pp. 429–36.
53. H. Wang, H. Li, H. Feng, W. Jiao, H. Zhu, S. Zhang, and Z. Jiang: *Mater Charact*, 2023, vol. 203, 113154.
54. N. Mebarki, D. Delagnes, P. Lamesle, F. Delmas, and C. Levaillant: *Mater. Sci. Eng. A*, 2004, vol. 387–389, pp. 171–75.
55. S. Morito, J. Nishikawa, and T. Maki: *ISIJ Int.*, 2003, vol. 43, pp. 1475–477.
56. K.S. Cho and H. Kwon: *Met. Mater. Int.*, 2017, vol. 23, pp. 632–38.
57. R.A. Mesquita and H.-J. Kestenbach: *Int. Heat Treat. Surf. Eng.*, 2010, vol. 4, pp. 145–51.
58. D. Delagnes, P. Lamesle, M.H. Mathon, N. Mebarki, and C. Levaillant: *Mater. Sci. Eng. A*, 2005, vol. 394, pp. 435–44.
59. E. Kozeschnik and H.K.D.H. Bhadeshia: *Mater. Sci. Technol.*, 2008, vol. 24, pp. 343–47.
60. G. Miyamoto, J.C. Oh, K. Hono, T. Furuhara, and T. Maki: *Acta Mater.*, 2007, vol. 55, pp. 5027–38.
61. A. Röttger, J. Boes, F. Großwendt, and S. Weber: *Addit. Manuf.*, 2023, vol. 61, 103292.
62. K. Schröcker, M. Fichtl, B. Bax, D. Scheider, M. Reisacher, and A. Prihodovsky: *Procedia CIRP*, 2022, vol. 111, pp. 228–32.
63. S. Amirabdollahian, M. Perini, T. Tugce, P. Bosetti, and A. Molinari: in *The 12th Tooling Conference & Exhibition*, Örebro, Sweden, 2022, p. 116.
64. F. Deirmina, P.A. Davies, N. Dixit, R. Siriki, and M. Pellizzari: *Metall. and Mater. Trans. A*, 2022, vol. 53, pp. 2642–51.
65. L. Wu, S. Das, W. Gridin, S. Leuders, M. Kahlert, M. Vollmer, and T. Niendorf: *Adv. Eng. Mater.*, 2021, vol. 23, p. 2100049.
66. Y. He, M. Zhong, J. Beuth, and B. Webler: *J. Mater. Process. Technol.*, 2020, vol. 286, 116802.